Aerosol vertical distribution and optical properties over China from long-term satellite and ground-based remote sensing

Pengfei Tian[1, 2], Xianjie Cao[1], Lei Zhang[1*], Naixiu Sun[1], Lu Sun[2], Timothy Logan[2], Jinsen Shi[1], Yuan Wang[3], Yuemeng Ji[2,4], Yun Lin[2], Zhongwei Huang[1], Tian Zhou[1], Yingying Shi[1], Renyi Zhang[2*]

[1]Key Laboratory for Semi-Arid Climate Change of the Ministry of Education, College of Atmospheric Sciences, Lanzhou University, Lanzhou 730000, China

[2]Department of Atmospheric Sciences, Texas A&M University, College Station, Texas 77843, USA

[3]Jet Propulsion Laboratory, California Institute of Technology, Pasadena, California 91125, USA

[4]Institute of Environmental Health and Pollution Control, School of Environmental Science and Engineering, Guangdong University of Technology, Guangzhou 510006, China

Correspondence to: L. Zhang (zhanglei@lzu.edu.cn) and R. Zhang (renyi-zhang@tamu.edu)

Abstract. The seasonal and spatial variations of vertical distribution and optical properties of aerosols over China are studied using long-term satellite observations from the Cloud–Aerosol Lidar with Orthogonal Polarization (CALIOP) and ground-based lidar observations and the Aerosol Robotic Network (AERONET) data. The CALIOP products are validated using the ground-based lidar measurements at the Semi-Arid Climate and Environment Observatory of Lanzhou University (SACOL). The Taklimakan Desert and Tibetan Plateau regions exhibit the highest depolarization and color ratios because of the natural dust origin, whereas the North China Plain, Sichuan Basin and Yangtze River Delta show the lowest depolarization and color ratios because of aerosols from secondary formation of the anthropogenic origin. Certain regions, such as the North China Plain in spring and the Loess Plateau in winter, show intermediate depolarization and color ratios because of mixed dust and anthropogenic aerosols. In the Pearl River Delta region, the depolarization and color ratios are similar to but higher, respectively, than those of the other polluted regions because of combined anthropogenic and marine aerosols. Long-range transport of dust in the middle and upper troposphere in spring is well captured by the CALIOP observations. The seasonal variations in the aerosol vertical distributions reveal efficient transport of aerosols from the atmospheric boundary layer to the free troposphere because of summertime convective mixing. The aerosol extinction lapse rate in autumn and winter are more positive than those in spring and summer, indicating trapped aerosols within the boundary layer because of more stable meteorological conditions. More

than 80% of the column aerosols are distributed within 1.5 km above the ground in winter, when the aerosol extinction lapse rate exhibits a maximum seasonal average in all study regions except for the Tibetan Plateau. The aerosol extinction lapse rates in the polluted regions are higher than those of the less polluted regions, indicating a stabilized atmosphere by absorbing aerosols in the polluted regions. Our results reveal that the satellite and ground-based remote sensing measurements provide the key information on the long-term seasonal and spatial variations in the aerosol vertical distribution and optical properties, regional aerosol types, long-range transport, and atmospheric stability, which can be utilized to more precisely assess the direct and indirect aerosol effects on weather and climate.

1 Introduction

Atmospheric aerosols affect the radiative budget of the Earth–atmosphere system by direct interaction with solar radiation through scattering and absorption (Boucher et al., 2013). Also, by acting as cloud condensation nuclei (CCN) or ice nuclei (IN), aerosols alter cloud formation, albedo, lifetime, precipitation efficiency, and lightning activity, indirectly influencing weather and climate (Nesbitt et al., 2000; Garrett and Zhao, 2006; Li et al., 2008; Garrett et al., 2010; Li et al., 2011; Rosenfeld et al., 2014; Wang et al., 2014; Zhao and Garrett, 2015). Currently, the understanding of the aerosol effects remains uncertain, since representation of the aerosol and cloud processes by atmospheric numerical models is difficult, leading to the largest uncertainty in climate projections (Zhang et al., 2007; Boucher et al., 2013; Xie et al., 2013). Also, absorbing aerosols heat the air and stabilize the atmosphere, exerting a negative impact on air quality (Wang et al., 2013a), and proper representation of the particle mixing state is key to assess the atmospheric stability under polluted environments (Kahlizov et al., 2009; Peng et al., 2016). Furthermore, aerosols provide surfaces for heterogeneous reactions that play a central role in the particles growth, transformation, and properties (Zhang et al., 1996; Zhao et al., 2006). Typically, aerosols under polluted conditions contain a complex mixture of inorganic and organic species and are internally or externally mixed (Wang et al., 2016).

The lack of information on the vertical distributions of aerosols is one of the main underlying factors for uncertainties in the aerosol direct radiative forcing, since the predictions from atmospheric models typically suffers from large variability (Huneeus et al., 2011). Lidar is a useful tool to provide the vertical distribution of atmospheric aerosols (Sugimoto and Huang, 2014), including ground-based lidars, aircraft-based lidars, and the Cloud–Aerosol Lidar with Orthogonal Polarization (CALIOP) onboard the Cloud–Aerosol Lidar and Infrared Pathfinder Satellite Observation (CALIPSO) satellite (Winker et al., 2009). The CALIOP observations are consistent with the Moderate Resolution Imaging Spectroradiometer (MODIS) results for the geographical patterns and seasonal variations (Yu et al., 2010). However, the CALIOP aerosol optical depth (AOD) presents an underestimation because of the challenge for thin aerosol layer detection (e.g., Winker et al., 2013; Liu et al., 2014; Papagiannopoulos et al., 2016). The CALIOP AOD over China has been validated using MODIS and the Aerosol Robotic Network (AERONET) data (Liu et al., 2014). The climatological extinction profiles obtained by CALIOP and the European Aerosol Research Lidar Network (EARLINET) are consistent, despite the issue of a slight underestimation (Papagiannopoulos et al., 2016). However, there exist few studies focusing on validating the CALIOP observed aerosol vertical distributions over China, especially on the climatology of the seasonal average vertical profiles of the aerosol extinction coefficient.

The seasonal aerosol vertical distribution over China has been studied using ground-based lidar observations at several sites (He et al., 2008; Huang et al., 2008a; Wu et al., 2011; Cao et al., 2013). The three-dimensional structure of aerosols over China has been estimated using the frequency of aerosol occurrence derived from CALIOP observations (Guo et al., 2016a). However, the seasonal aerosol extinction coefficient profiles in representative regions over China have not yet been studied. The diverse natural and anthropogenic aerosol sources as well as the geographical and meteorological conditions and transport pathways make China a unique natural laboratory for examination of seasonal dust particles, anthropogenic pollution, and aerosols of mixed types (Zhang et al., 2015). For example, spring dust particles originating from the source regions in the northwest of China are transported to the middle and upper troposphere (Wu et al., 2011; Wang et al., 2013b) and to the downstream regions (Logan et al., 2010; Huang et al., 2015a). Long-range transported particles are typically internally or externally mixed with other aerosol constituents along their transport pathway (Logan et al., 2013; Pan et al., 2015), because of atmospheric processing (Zhang and Zhang, 2005; Zhang et al., 2008). The high contribution of secondary aerosols represents a major characteristic during haze events in China (Guo et al., 2014; Zhang et al., 2015), because of efficient photochemical and particle-phase reactions of organic and inorganic spices under polluted conditions (e.g., Lei et al., 2001; Zhang et al., 2002; Suh et al., 2003; Yue et al., 2010). Also, hygroscopic aerosols increase AOD at higher relative humidity (Qiu and Zhang, 2012; 2013). The vertical

distribution of aerosols is governed by transport, which is related to atmospheric stability. For example, effective convection in summer transports aerosols from the planetary boundary layer to the free troposphere (He et al., 2008; Cao et al., 2013), but stable atmospheric conditions in winter contribute to higher air pollution accumulation near the surface (Zhang et al., 2008). Also, air pollution is further enhanced by the aerosol–planetary boundary layer feedback in China (Peng et al., 2016; Petäjä et al., 2016; Yang et al., 2016). The seasonal aerosol mass size distribution over China has been found to be bimodal lognormal by using Nine-stage Anderson Sampler, with a maximum coarse mode in spring and a maximum fine mode in winter (Xin et al., 2015). In situ aerosol composition measurements over 16 urban and rural sites across China have suggested that the seasonal maximum concentrations of most aerosol species occur in winter, whereas the seasonal maximum concentrations of dust aerosol occur in spring (Zhang et al., 2012).

The lidar-observed aerosol depolarization and color ratios are the key parameters in aerosol and cloud characterizations (Sugimoto et al., 2002; Zhou et al., 2013). The color ratio (or wavelength ratio), defined as the ratio between 1064 nm and 532 nm backscatter, is positively related to the aerosol size (Sasano and Browell, 1989). The backscattering linear depolarization ratio is defined as the ratio between the perpendicular and parallel backscatter intensities, and the ratio is zero for spherical aerosols and larger for non-spherical aerosols. The depolarization ratio is used as an aerosol subtyping parameter in the CALIPSO

classification algorithm (Omar et al., 2009). CALIOP has continuously conducted observations of the global atmosphere aerosol vertical distribution since June 2006 (Winker et al., 2009).

In this study, we have investigated the regional climatological aerosol vertical distributions and optical properties over eight representative regions in China. Our study focuses on the seasonal aerosol vertical extinction profiles on a regional scale and the seasonal optical properties of dust particles, anthropogenic aerosols, and aerosols of mixed types. We also examine the interaction between aerosols and atmospheric stability by analyzing the aerosol extinction lapse rate. The study regions, observation sites, instruments, data processing and validating are described in section 2. The spatial distributions of seasonal column AOD are presented in section 3. The seasonal aerosol optical properties and vertical distributions are analyzed and discussed in sections 4 and 5, respectively.

2 Data and methodology

2.1 Study regions

In our study, eight study regions (Fig. 1 and Table 1) and 21 AERONET sites (Fig. S1 and Table S1) are selected to represent the diverse aerosol types in China. The Taklimakan Desert region is dominated by dust particles year round (Ge et al., 2014). In the Tibetan Plateau, aerosols are mainly transported from the Taklimakan Desert during spring and summer (Liu et al., 2008; Jia et al., 2015). The Loess Plateau region is dominated by dust particles in spring, anthropogenic aerosols in summer, and the mixtures of dust with anthropogenic pollution in

winter (Wang et al., 2013b). The Northeast China Plain is one of the cleanest regions in China, because it presents less natural dust and anthropogenic pollution (Luo et al., 2014; Tao et al., 2015). The Sichuan Basin, North China Plain, and Yangtze River Delta are dominated by anthropogenic pollution (Huang et al., 2011; Zhang et al., 2012). Also, the North China Plain contains anthropogenic dust year round and transported natural dust in spring (Logan et al., 2013; Huang et al., 2015b). The air quality and pollution dispersal over the Pearl River Delta are controlled by specific meteorological conditions, and the Pearl River Delta aerosols are dominated by anthropogenic pollution and a small fraction of marine aerosols (Hara et al., 2011; Xu et al., 2015).

2.2 CALIOP data and processing

A comparison of the CALIOP observations with the MODIS products suggests that the CALIOP version 3 products provide a consistent and representative mean regional and seasonal aerosol load and distribution compared with the version 2 products (Koffi et al., 2012). The CALIOP version 3 level 2 aerosol and cloud products from June 2006 to January 2016 are employed in this study. All of the results in this study are under cloud-free conditions, i.e., no cloud layer in the 5 km cloud layer products. The parameters of the aerosol layers, such as layer-integrated aerosol color ratio, layer-integrated aerosol depolarization ratio, and layer top and base altitudes, are derived from the CALIOP 5 km aerosol layer products. The column aerosol AOD is also derived from the CALIOP 5 km aerosol layer products, and the average

seasonal AOD is calculated using the following quality control procedures: (1) cloud free; (2) $0 \leq AOD_{532nm} \leq 3.0$; (3) $-100 \leq CAD\_Score \leq -20$; (4) $Ext\_QC = 0, 1$; and (5) $0 < AOD_{532nm,unc}/AOD_{532nm} \leq 100\%$, where AOD_{532nm} is the aerosol optical depth at 532 nm wavelength, CAD_Score is the cloud-aerosol discrimination score, Ext_QC is the extinction quality control flags, and $AOD_{532nm,unc}$ is the uncertainty of AOD_{532nm}. The seasonal aerosol extinction vertical profiles are derived from the CALIOP 5 km aerosol profile products with similar quality control procedures as in Winker et al. (2013): (1) $-100 \leq CAD\_Score \leq -20$; (2) $Ext\_QC = 0, 1$; (3) fill values representing clear sky conditions are assigned an extinction value of 0.0 km^{-1}; (4) range bins with uncertainty of 99.9 km^{-1} and bins at lower altitudes in the profile are rejected; and (5) extinction values near the surface less than −0.2 km^{-1} are ignored. Higher thresholds are adopted for the CALIOP data processing during daytime hours than nighttime hours because of the daytime background solar illumination (Winker et al., 2013). Thus, weakly scattering aerosol layers that are detected at night may not be detected during the daytime. Therefore, the averaged daytime extinction profiles are higher and tend to be noisier than the nighttime profiles. Consequently, the nighttime CALIOP aerosol profiles and layer products are used in this study.

Similar to the temperature lapse rate, the aerosol extinction (coefficient) lapse rate (γ_{ext}) is defined as,

$$\gamma_{ext} = -d\sigma(z)/dz \quad (1)$$

where $\sigma(z)$ is the extinction coefficient at the height of z. The unit of γ_{ext} is km^{-2} (km^{-1}/km). Stable meteorological conditions are unfavorable for aerosol vertical transport (Kipling et al., 2016) and lead to a high positive aerosol extinction lapse rate. The extinction lapse rate is more applicable to a climatological aerosol vertical profile rather than an instantaneous profile, because an elevated aerosol layer in the instantaneous profile leads to a negative aerosol extinction lapse rate. The ratio of AOD with 1.5 km above the ground to the column AOD, $R_{AOD,1.5km}$, is derived from the average extinction profiles:

$$R_{AOD,1.5km} = \sum_{k=base}^{base+1.5} \sigma(z_k) / \sum_{k=base}^{top} \sigma(z_k) \quad (2)$$

2.3 Ground-based lidar and extinction retrieval

The Semi-Arid Climate and Environment Observatory of Lanzhou University (SACOL, 35.946 °N, 104.137 °E, and 1965.8 m ASL) is an international research observatory located in the semi-arid region of the Loess Plateau in northwest China (Huang et al., 2008b). Lidar observations were performed by a National Institute for Environmental Studies (NIES) depolarization lidar (Huang et al., 2010) from October 2009 to August 2012. The lidar data is denoised using the empirical mode decomposition (EMD)-based method according to Tian et al. (2014). The lidar equation (Fernald, 1984) is as follows:

$$P(z) = ECz^{-2}[\beta_1(z) + \beta_2(z)]T^2(z) \quad (3)$$

where $P(z)$ is the lidar backscattering return signal at the height of z, E is an output energy monitor pulse, C is a calibration constant, $\beta_1(z)$ is the aerosol backscattering coefficient,

$\beta_2(z)$is the molecule backscattering coefficient, and $T(z) = exp\{-\int_0^z[\sigma_1(z) + \sigma_2(z)]\,dz\}$ is the transmittance. $\sigma_1(z)$ is the aerosol extinction coefficient, and $\sigma_2(z)$ is the molecule extinction coefficient. The ratio between $\sigma_1(z)$ and $\beta_1(z)$ (known as the lidar ratio or extinction to backscattering ratio) is pre-assigned to solve the equation, because this equation is not closed due to the two unknowns $\sigma_1(z)$ and $\beta_1(z)$. If the AOD is simultaneously observed using a sun photometer, the aerosol extinction coefficient profile can be retrieved using the AOD-constrained Fernald (1984) method, as described in Takamura et al. (1994) and Huang et al. (2010). The aerosol extinction coefficients retrieved from the AOD-constrained retrieval method is subjected to less uncertainty because the lidar ratio assumption is not required.

2.4 AERONET sites and data processing

All AERONET sites with an observation of more than 3 months in the representative regions were selected (Fig. S1 and Table S1). There were 17 sites in the Loess Plateau, the North China Plain, the Pearl River Delta, the Tibetan Plateau, and the Yangtze River Delta regions included in our study. In addition, four desert sites in Hexi Corridor of Gansu of the northwest China were selected to represent dust aerosols. A large amount of the version 2, level 2 AOD products was available, while the inversion products were limited at several sites. The inversion data amount of NAM_CO site in the Tibetan Plateau region and the sites in Hexi Corridor of Gansu was limited for robust climatological results.

The aerosol volume size distribution and single scattering albedo (SSA) data from the Aerosol Robotic Network (AERONET) are utilized to characterize the typical aerosol types at the SACOL (35.946°N, 104.137°E), Beijing (39.98°N, 116.38°E), and Taihu (31.42°N, 120.22°E) sites (Fig. 1). Data are available from 28 July 2006 to 10 August 2012 for SACOL, from 9 March 2001 to 23 March 2015 for Beijing, and from 6 September 2005 to 4 October 2012 for Taihu. The aerosol size distribution and SSA are the key parameters in aerosol classification (Li et al., 2007). The aerosol classification method by Logan et al. (2013) is also considered in this study. This method is based on two parameters from the AERONET observations: the Ångström exponent ($\alpha_{440-870}$) and single scattering co-albedo ($\omega_{\mathrm{oabs440}}$). The Ångström exponent is a good indicator of the size of aerosols, and a threshold of $\alpha_{440-870} = 0.75$ is used to define fine ($\alpha_{440-870} > 0.75$) and coarse mode ($\alpha_{440-870} < 0.75$) aerosols (Eck et al., 2005). The single scattering co-albedo is the ratio of absorption to extinction aerosol optical depths. $\omega_{\mathrm{oabs440}} = 0.07$ is set as a threshold value to define weakly ($\omega_{\mathrm{oabs440}} < 0.07$) and strongly ($\omega_{\mathrm{oabs440}} > 0.07$) absorbing aerosols. The weakly and strongly absorbing pollution, mineral dust, and biomass burning aerosols are classified according to the method by Logan et al. (2013).

2.5 Validation of the CALIOP extinction profiles

The aerosol extinction coefficients in the free troposphere are typically underestimated under clean conditions (Winker et al., 2013). The climatological extinction profiles obtained

by CALIOP and the European Aerosol Research Lidar Network (EARLINET) are consistent, although the CALIOP results show a slight underestimation (Papagiannopoulos et al., 2016). Validation of seasonal CALIOP aerosol extinction coefficient profiles using ground-based lidar observations at SACOL is carried out in this study. The nighttime CALIOP observations with a distance of less than 100 km from SACOL are averaged to calculate the seasonal extinction coefficient profiles using the data quality control procedures described in section 2.2. Hourly average NIES lidar extinction profiles are retrieved using the AOD-constrained Fernald method developed by Huang et al. (2010). The seasonal extinction profiles are derived from the hourly averages. The seasonal vertical distributions are well captured by the CALIOP observations (Fig. 2). The NIES lidar spring extinction profile is very close to that observed by a Micro-Pulse Lidar (MPL) at SACOL in the spring of 2007 (Huang et al., 2008a). The seasonal aerosol extinction profiles over SACOL have been studied using the observations from a CE370-2 lidar (Cao et al., 2013). However, because observations under dusty conditions were excluded from the average, the seasonal average extinction profiles of the CE370-2 lidar are smaller than the NIES profiles.

3 Spatial distribution of aerosol optical depth

The combined daytime and nighttime seasonal average AOD over China from the CALIOP observations is shown in Fig. 3. The CALIOP AOD is consistent with the MODIS AOD (Luo et al., 2014; Tao et al., 2015), Multi-angle Imaging Spectroradiometer (MISR)

AOD (Qi et al., 2013), and ground-based AOD (Che et al., 2015) with regard to the geographical patterns and seasonal variations. CALIOP provides a full coverage of China, including the Tibetan Plateau and Taklimakan Desert regions with a 1.0° × 2.5° latitude-longitude grid, which is an important advantage over the passive satellites. The seasonal AOD hotspots over the Taklimakan Desert, North China Plain, Sichuan Basin, and Yangtze River Delta are clearly evident in the CALIOP observations. The AOD hotspots over China coincide with high $PM_{2.5}$ (particles with the aerodynamic diameter smaller than 2.5 μm) concentrations (Zhang and Cao, 2015), which are also associated with population hotspots over China (Ma et al., 2016), except in the Taklimakan Desert region.

Dust represents the main natural aerosol type over northwest China, especially in spring (Wang et al., 2013b). In situ measurements over 16 sites across China have revealed that 35% of the aerosols are composed of mineral dust (Zhang et al., 2012). High ratios of the dust-only AOD to the total AOD are centered on the dust source regions in northwest China (Fig. S2a). The ratio of the dust-only to total AOD is also high over the Tibetan Plateau, because of transported dust from the Taklimakan Desert (Liu et al., 2008; Jia et al., 2015). Mixed dust with anthropogenic pollution/biomass burning aerosols are classified as polluted dust in the CALIPSO aerosol subtyping algorithm (Omar et al., 2009). A hot spot of the polluted-dust AOD to total AOD ratio is in the North China Plain (Fig. S2b). The polluted dust in the North China Plain is considered to be anthropogenic dust (Huang et al., 2015b).

4 Aerosol optical properties over the representative regions

The CALIOP layer-integrated volume depolarization ratio (δ'_{layer}) and layer-integrated volume color ratio (χ'_{layer}) are calculated from:

$$\delta'_{layer} = \sum_{k=top}^{base} \beta_{532,\perp}(z_k) / \sum_{k=top}^{base} \beta_{532,\parallel}(z_k) \quad (4)$$

$$\chi'_{\mathrm{layer}} = \sum_{\mathrm{k=top}}^{\mathrm{base}} \beta_{1064,\mathrm{k}} / \sum_{\mathrm{k=top}}^{\mathrm{base}} \beta_{532,\mathrm{k}} \quad (5)$$

where $\beta_{532,\perp}(z_k)$ and $\beta_{532,\parallel}(z_k)$ refer to the polarized and depolarized attenuated backscatter signals, respectively, and $\beta_{1064,\mathrm{k}}$ and $\beta_{532,\mathrm{k}}$ refer to the attenuated backscatter coefficients at 1064 and 532 nm wavelengths, respectively. The layer-integrated volume depolarization ratio δ'_{layer} and layer-integrated volume color ratio χ'_{layer} are then corrected to the layer-integrated aerosol (or particle) depolarization ratio δ_{layer} and layer-integrated aerosol (or particle) color ratio χ_{layer} (Omar et al., 2009). The volume depolarization and color ratio include the molecular scattering contribution, as widely used in the aerosol classification (Omar et al., 2009; Mielonen et al., 2009; Huang et al., 2015b). Dust particles are composed of non-spherical, coarse-mode-dominated mineral dust (Kandler et al., 2011), while anthropogenic pollution aerosols are fine-mode-dominated particles with a spherical shape (Sugimoto et al., 2002; Omar et al., 2005). The dust particles have a volume depolarization ratio of higher than 0.2, while anthropogenic pollution aerosols have a volume depolarization ratio of lower than 0.1 (Xie et al., 2008; Nemuc et al., 2013). Dust particles are internally or externally mixed with other aerosol types along their transport pathway (Pan et al., 2015). Marine aerosols are

dominated by sea salts, which are coarse-mode-dominant but smaller than the desert dust (Porter and Clarke, 1997). The color ratios of sea salt aerosols are higher than those of sulfate aerosols (Sugimoto et al., 2002), and the aerosol depolarization ratios for marine aerosols range from 0.01 to 0.03 (Groß et al., 2011).

The scatter plots for layer-integrated aerosol color ratios versus layer-integrated aerosol depolarization ratios for the eight study regions are shown in Fig. 4. In order to better compare aerosol optical properties in different study regions, the ratio of the data point number in a 0.067×0.020 color ratio-depolarization ratio grid to the maximum data point number in a grid in each region (referred to as the number density of the color ratio versus depolarization ratio data points) is depicted by the colors in Fig. 4. The green, yellow and red data points, which have a number density of 0.4 to 1.0, account for more than 85% of the total data points. Dust-dominated aerosols are scattered in the upper right area in Figs. 4 (a) and (b) (i.e., in the Taklimakan Desert and Tibetan Plateau regions), corresponding to large and non-spherical particles. In contrast, anthropogenic aerosols dominated by secondary formation are scattered in the lower left area in Figs. 4 (d), (e), (f) and (g) (i.e., in the Northeast China Plain, Sichuan Basin, North China Plain, and Yangtze River Delta regions), corresponding to small and spherical particles. For the Loess Plateau region, the data points are scattered from the lower left all the way to the upper right, because of mixed particles from anthropogenic pollution and natural dust. The data points in the Pearl River Delta show the similar scattered pattern, but

with a higher color ratio than those of anthropogenic pollution aerosols, because of the existence of a fraction (about 20%) of larger-sized marine sea salt aerosols (Xu et al., 2015).

To better understand the optical proprieties for the different aerosol types and their mixtures, the seasonal average layer-integrated aerosol color ratios versus the layer-integrated aerosol depolarization ratios of the eight representative study regions are present in Fig. 5. The seasonal scatter plots for the layer-integrated aerosol color ratios versus layer-integrated aerosol depolarization ratios for the eight study regions are shown in Figs. S3-10. The spring regional average depolarization ratios are higher than those of the other seasons in the same region and higher than 0.1, except in the Pearl River Delta region. The summer regional average depolarization ratios are lower than those during the other seasons in the same region and lower than 0.1, except for the regions in northwest China, i.e., the Taklimakan Desert, Tibetan Plateau, and Loess Plateau. All of the seasonal average data points of the Taklimakan Desert and Tibetan Plateau are scattered in the upper right area (with large and non-spherical particles), whereas those of the Northeast China Plain and Pearl River Delta are scattered in the lower left area (with small and spherical particles). For the regions dust plays an important role in spring and anthropogenic pollution dominates in summer, i.e., the Loess Plateau, North China Plain, Sichuan Basin, and Yangtze River Delta, the data points are scattered along the regression line from the lower left to the upper right in the sequence of summer, autumn, winter

and spring. The depolarization ratio differences between the spring and summer averages for these four regions are in the range of 0.11-0.12.

The AERONET observed Ångström exponent versus AOD provides a simple yet useful classification of the aerosol optical properties in the different regions (Fig. 6). NAM_CO is a background site located in the Tibetan Plateau region, with the lowest AOD. The sites in the Hexi Corridor of Gansu correspond to coarse mode dust-dominant aerosols, with the lowest Ångström exponent. The sites in the Yangtze River Delta and the Pearl River Delta regions exhibit the highest Ångström exponent, mainly caused by fine mode aerosols from anthropogenic pollution. The natural dust and aerosols from anthropogenic pollution are noticeably distinct in the Loess Plateau and the North China Plain regions. Aerosols dominated by anthropogenic pollution in the North China Plain region exhibit the highest AOD.

As shown in Fig. 7, spring dust is clearly evident in the Loess Plateau and the North China Plain regions that have the highest seasonal coarse modes and an increasing spectral SSA trend and in the Yangtze River Delta, albeit at a less extent. During summer, fine mode aerosols dominate the regions of North China Plain, Yangtze River Delta, and Pearl River Delta, with a decreasing spectral SSA trend. The Loess Plateau region also shows a decreasing spectral SSA trend in summer, although the coarse mode aerosols dominate this region. Aerosols in autumn and winter in the Loess Plateau, North China Plain, and Yangtze River

Delta regions show a non-monotonic feature in the spectral SSA, indicating mixed aerosol types (Li et al., 2015).

The dust-dominant aerosols of spring SACOL, anthropogenic pollution-dominated aerosols of summer Beijing and summer Taihu, and aerosols of mixed type of spring Beijing are clearly represented by AERONET observations (Figs. 8 and 9). Most of the spring aerosols over SACOL are of large size ($\alpha_{440-870} < 0.75$) and strongly absorbing ($\omega_{oabs440} > 0.07$) (Fig. 9). The natural dust-dominated SACOL aerosols in spring are mainly in the coarse mode and present an increasing spectral SSA trend (Fig. 8). Aerosols are dominated by anthropogenic pollution during the summer in Beijing and Taihu, with a relatively higher fine mode peak in the size distribution and a decreasing spectral SSA trend. Aerosols at the Beijing site are more absorbing, with a relatively higher coarse mode and lower fine mode than those at the Taihu site. Aerosols in Beijing during spring are of the mixed type, which are dominated by dust and anthropogenic aerosols with high absorption. Therefore, the spring Beijing aerosols have a similar coarse mode and a higher fine mode than those of the spring SACOL aerosols. The mixed aerosol types in Beijing in spring exhibit a spectral SSA trend that differs from both dust and anthropogenic aerosols.

5 Aerosol vertical distributions over the representative regions

As a major characteristic of aerosols over China, spring dust is transported to the middle and higher troposphere, which is well reflected from the CALIOP observations on a regional

scale (Fig. 10). Strong vertical mixing in summer transports more aerosols from the atmospheric boundary layer to the free troposphere, including the Taklimakan Desert dust. In contrast, stable meteorological conditions in autumn and winter trap more aerosols within the boundary layer. About 80% of the column aerosols in winter are distributed within 1.5 km above the ground (Table 2), and the extinction lapse rates (Eq. 1) increase to over 0.15 km^{-2} (Fig. 11).

To better understand the aerosol properties in the Taklimakan Desert region, the CALIOP detected number and depth of the aerosol layers with a layer base within 2 km above the ground from June 2006 to January 2016 are calculated. There are 6904, 12727, 19445 and 14510 aerosol layers, with a layer depth (average±standard deviation) of 2.464 ± 1.107 km, 2.396 ± 1.336 km, 1.705 ± 1.014 km, and 0.960 ± 0.536 kmin spring, summer, autumnand winter, respectively. In the Taklimakan Desert region, spring dust aerosols show the highest seasonal average depolarization ratio of 0.32 ± 0.08 (Fig. 5), the highest layer depth, and the largest extinction coefficients (Fig. 10a). Dust is efficiently transported to the upper troposphere in summer, because of strong winds (Ge et al., 2016). The Taklimakan Desert region exhibit the lowest boundary layer height in winter (Guo et al., 2016b). Therefore, the winter dust aerosols are trapped within the boundary layer and mixed with anthropogenic pollution, with a thinner layer depth and a lower average depolarization ratio of 0.23 ± 0.10. In addition, 89% of the total column aerosols are distributed within 1.5 km above the ground in winter (Table 2).

The Tibetan Plateau is a clean region with low anthropogenic aerosol loading, but Taklimakan Desert dust can be transported to the Tibetan Plateau in spring and summer (Liu et al., 2008; Jia et al., 2015). The spring and summer extinction profiles of the Tibetan Plateau aerosols are much larger than the autumn and winter profiles. CALIOP-detected nighttime aerosol layer numbers over the Tibetan Plateau are 16502, 11579, 6667 and 8030 in spring, summer, autumn and winter, respectively. The maximum spring and summer average extinction coefficients are approximately 0.017 km^{-1} at 5.0 km height, whereas the maximum autumn and winter coefficients are less than 0.005 km^{-1}. Note that the extinction coefficients may be overestimated in the Tibetan Plateau, because the weakly scattering aerosol layers may not be detected by CALIOP.

Aerosols are mainly trapped within the boundary layer in autumn and winter over the Loess Plateau region (Table 2 and Fig. 10c). Transported spring dust causes higher extinction coefficients in the middle and upper troposphere. Summer extinctions are larger than those for the other seasons in the Loess Plateau region, which may be attributable to more hygroscopic aerosols due to more abundant water vapor and higher temperatures in summer (Su et al., 2014). The seasonal aerosol vertical distributions over the Northeast China Plain region (Fig. 10d) are similar to that of the Loess Plateau but with lower extinctions because of both lower natural dust and lower anthropogenic aerosol loadings (Luo et al., 2014).

The Sichuan Basin, North China Plain, and Yangtze River Delta regions contain high levels of anthropogenic pollution, and the aerosol extinctions are higher than those of the spring Taklimakan Desert dust (Fig. 10). High anthropogenic emissions, efficient secondary aerosol formation (Zhang et al., 2015), and stable meteorological conditions (Miao et al., 2015) contribute to large aerosol loadings within the atmospheric boundary layer in these regions. The aerosol extinctions within the atmospheric boundary layer are large in summer and winter for the North China Plain and Yangtze River Delta, whereas the values for the Sichuan Basin are relatively low in summer. The SO_2 and NO_2 concentrations over the Sichuan Basin are lower than those over the North China Plain and Yangtze River Delta regions (Wang et al., 2015; Cui et al., 2016), and the Sichuan Basin region also corresponds to fewer sunny days (Liu et al., 2010), leading to low photochemical activity. Moreover, strong vertical mixing in summer also transports aerosols vertically in the Sichuan Basin region.

Although local anthropogenic pollution plays a major role in the Pearl River Delta region, the northwest winter monsoon transports continental aerosols, and the southeast summer monsoon transports marine aerosols to this region (Wu et al., 2013). The aerosol extinction coefficients within the planetary boundary layer in autumn and winter are much higher than those in spring and summer (Fig. 10h). A lower planetary boundary layer height in autumn and winter (Guo et al., 2016b) also contributes to higher aerosol loading near the surface. It is worth noting that an elevated aerosol layer in the altitudes of 2 to 5 km is evident in the Pearl River Delta region

in spring. Using observation of a multi-wavelengths Raman and depolarization lidar and backward trajectory analysis, Heese et al. (2016) have shown a similar characteristic, indicating that particles in this region are pollution mixtures locally and regionally produced.

Convective transport has been suggested to be an important factor that controls the vertical distribution of aerosols (Kipling et al., 2016). It has been suggested that absorbing aerosols (including black carbon) play an important role in determining the atmospheric stability (Wang et al., 2013a; Peng et al., 2016). Light absorption and scattering of the atmospheric aerosols heat the air and decrease the surface temperature, enhancing accumulation of air pollution (Ding et al., 2016; Petäjä et al., 2016; Yang et al., 2016). The absorption aerosol optical depth (AAOD) over the polluted regions (i.e., the Sichuan Basin, North China Plain, Yangtze River Delta, and Pearl River Delta) is much higher than the other regions in China (Gustafsson and Ramanathan, 2016). The extinction lapse rates over the polluted regions are higher than the less polluted regions (Fig. 11). The extinction lapse rates are higher than 0.2 km^{-2} in the polluted regions, while those in the less polluted regions are generally lower than 0.1 km^{-2}. The autumn and winter extinction lapse rates are higher than those of the spring and summer rates for most regions, explainable by a lower atmospheric boundary layer height (Guo et al., 2016b) and a higher fraction of black carbon aerosols (Schleicher et al., 2013) in autumn and winter than those in spring and summer. The extinction lapse rate in the Taklimakan Desert region shows a seasonal maximum in winter, when the

planetary boundary layer height is low (Guo et al., 2016b) and elevated black carbon aerosols from coal combustion for heating in winter. The spring extinction lapse in the Taklimakan Desert region is higher than those in summer and autumn, probably attributable to absorbing dust aerosols in spring.

6 Conclusions

The vertical aerosol distributions and optical properties are essential in assessing the aerosol direct and indirect radiative forcing, but few studies have reported these regional climatological data over China using combined long-term satellite and ground-based remote sensing observations. In this work, the CALIOP satellite products are validated using the ground-based lidar observations, and the CALIOP seasonal AOD spatial distribution is obtained. The CALIOP aerosol layer products and AERONET data are employed to evaluate the aerosol optical properties of the dust-dominated particles, anthropogenic pollution-dominated aerosols, and aerosols of the mixed types. The CALIOP aerosol profile products are used to study the seasonal and spatial variations in the aerosol extinction coefficients for eight representative regions over China.

The seasonal variations in the aerosol vertical distributions are well captured by the CALIOP observations, although the CALIOP aerosol extinctions represent an underestimation when compared with the ground-based lidar results at SACOL. The long-term column AOD and aerosol vertical distribution over the Tibetan Plateau, which are typically difficult to obtain

by passive satellites, are determined using the CALIOP observations. The AOD hotspots over China are consistently co-located with the hotspots of high $PM_{2.5}$ concentrations and population, except in the Taklimakan Desert region.

The dust-dominant Taklimakan Desert and Tibetan Plateau regions exhibit the highest depolarization ratios and the highest color ratios, whereas the anthropogenic pollution-dominated North China Plain, Sichuan Basin and Yangtze River Delta regions show the lowest depolarization ratios and the lowest color ratios. The spring North China Plain and the winter Loess Plateau show intermediate depolarization and color ratios because of the mixed natural dust and anthropogenic pollution particles. In the Pearl River Delta region, the depolarization and color ratios are similar to but higher, respectively, than those of the polluted regions because of the combined anthropogenic pollution and marine aerosols.

Long-range transport of dust in the middle and higher troposphere during the spring season is clearly evident in the CALIOP observed aerosol extinction coefficient profiles. The seasonal variations in aerosol vertical distributions indicate efficient transport of aerosols from the atmospheric boundary layer to the free troposphere because of summertime convective mixing, but stable meteorological conditions trap more aerosols within the boundary layer in autumn and winter. The aerosol extinction lapse rate is closely correlated to the atmospheric stability, with higher values in autumn and winter than spring and summer. More than 80% of the column aerosols are distributed within 1.5 km above the ground in winter, when aerosol

extinction lapse rate reaches a maximum seasonal average in all the study regions except for the Tibetan Plateau. For the polluted regions (i.e., the Sichuan Basin, North China Plain, Yangtze River Delta, and Pearl River Delta), the aerosol extinction lapse rates in the planetary boundary layer are higher than those of the less polluted regions (the Taklimakan Desert, Tibetan Plateau, Loess Plateau, and Northeast China Plain). Our results suggest that absorbing aerosols may contribute to the high aerosol extinction lapse rates in the heavily polluted regions.

Hence, we have for the first time presented the seasonal and spatial variations of the profiles of aerosol extinction coefficients and identified the dominant regional aerosol types over China, using combined long-term satellite and ground-based remote sensing observations. The vertical aerosol distributions and optical properties from our work facilitate more precise assessment of the direct and indirect aerosol effects in China on weather and climate (Wang et al., 2011; Wu et al., 2016).

7 Data availability

The CALIOP data is available from the National Aeronautics and Space Administration (NASA) site (http://www-calipso.larc.nasa.gov/tools/data_avail/). The NIES lidar data is available from the SACOL site (http://climate.lzu.edu.cn/data/data.asp) upon request. The sun photometer data is available from the AERONET website (http://aeronet.gsfc.nasa.gov/). The regional climatology products in the eight representative regions over China, the lidar profiles at SACOL, and the AERONET results data in this paper are available from the authors upon

request. The gridded climatology aerosol extinction coefficient profiles (not shown in this paper) and AOD over China with a 1.0° × 2.5° latitude-longitude grid, which can be used as model input or to test model results, are also available from the authors upon request.

Acknowledgements. This research was funded by the National Natural Science Foundation of China (41475008, 41521004, 41225018 and 41405113) and the Fundamental Research Funds for the Central Universities (lzujbky-2016-k06). P. Tian was supported by the China Scholarship Council as a visiting scholar at Texas A&M University from September 2015 to August 2016. The authors are grateful to the National Aeronautics and Space Administration (NASA) for providing the CALIPSO satellite data used in this study and SACOL for providing the ground-based lidar data. We also thank the AERONET program for its efforts to establish and maintain the SACOL, Beijing, and Taihu sites.

References

Boucher, O., D. Randall, P. Artaxo, C. Bretherton, G. Feingold, P. Forster, V.-M. Kerminen, Y. Kondo, H. Liao, U. Lohmann, P. Rasch, S.K. Satheesh, S. Sherwood, B. Stevens and X.Y. Zhang, 2013: Clouds and Aerosols. In: Climate Change 2013: The Physical Science Basis. Contribution of Working Group I to the Fifth Assessment Report of the Intergovernmental Panel on Climate Change [Stocker, T.F., D. Qin, G.-K. Plattner, M. Tignor, S.K. Allen, J. Boschung, A. Nauels, Y. Xia, V. Bex and P.M. Midgley (eds.)], Cambridge University Press, Cambridge, United Kingdom and New York, NY, USA.

Cao, X., Wang, Z., Tian, P., Wang, J., Zhang, L., and Quan, X.: Statistics of aerosol extinction coefficient profiles and optical depth using lidar measurement over Lanzhou, China since 2005-2008, J. Quant. Spectrosc. Ra., 122, 150-154, doi:10.1016/j.jqsrt.2012.09.016, 2013.

Che, H., Zhang, X.Y., Xia, X., Goloub, P., Holben, B., Zhao, H., Wang, Y., Zhang, X.C., Wang, H., Blarel, L., Damiri, B., Zhang, R., Deng, X., Ma, Y., Wang, T., Geng, F., Qi, B., Zhu, J., Yu, J., Chen, Q., and Shi, G.: Ground-based aerosol climatology of China: aerosol optical depths from the China Aerosol Remote Sensing Network (CARSNET) 2002–2013, Atmos. Chem. Phys., 15, 7619-7652, doi:10.5194/acp-15-7619-2015, 2015.

Cui, Y., Lin, J., Song, C., Liu, M., Yan, Y., Xu, Y., and Huang, B.: Rapid growth in nitrogen dioxide pollution over Western China, 2005–2013, Atmos. Chem. Phys., 16, 6207-6221, doi:10.5194/acp-16-6207-2016, 2016.

Eck, T.F., Holben, B.N., Dubovik, O., Smirnov, A., Goloub, P., Chen, H.B., Chatenet, B., Gomes, L., Zhang, X.Y., Tsay, S.C., Ji, Q., Giles, D., and Slutsker, I.: Columnar aerosol optical properties at AERONET sites in central eastern Asia and aerosol transport to the tropical mid-Pacific, J. Geophys. Res., 110, D06202, doi:10.1029/2004JD005274, 2005.

Fernald, F.G.: Analysis of atmospheric lidar observations: some comments, Appl. Optics, 23, 652-653, doi:10.1364/AO.23.000652, 1984.

Garrett, T. J., and Zhao, C.: Increased Arctic cloud longwave emissivity associated with pollution from mid-latitudes, Nature, 787-789, doi:10.1038/nature04636, 440(7085), 2006.

Garrett, T. J., Zhao, C., and Novelli P. C.:, Assessing the relative contributions of transport efficiency and scavenging to seasonal variability in Arctic aerosol, Tellus B, 62(3), 190-196, doi:10.1111/j.1600-0889.2010.00453.x, 2010.

Ge, J.M., Huang, J.P., Xu, C.P., Qi, Y.L., and Liu, H.Y.: Characteristics of Taklimakan dust emission and distribution: A satellite and reanalysis field perspective, J. Geophys. Res., 119, 11772-11783, doi:10.1002/2014JD022280, 2014.

Ge, J. M., Liu, H., Huang, J., and Fu, Q.: Taklimakan Desert nocturnal low-level jet: climatology and dust activity, Atmos. Chem. Phys., 16, 7773-7783, doi:10.5194/acp-16-7773-2016, 2016.

Groß, S., Tesche, M., Freudenthaler, V., Toledano, C., Wiegner, M., Ansmann, A., Althausen, D., and Seefeldner, M.: Characterization of Saharan dust, marine aerosols and mixtures of

biomass-burning aerosols and dust by means of multi-wavelength depolarization and Raman lidar measurements during SAMUM 2, Tellus B, 63, 706-724, doi:10.1111/j.1600-0889.2011.00556.x, 2011.

Guo, J., Liu, H., Wang, F., Huang, J., Xia, F., Lou, M., Wu, Y., Jiang, J.H., Xie, T., Zhaxi, Y., and Yung, Y.L.: Three-dimensional structure of aerosol in China: A perspective from multi-satellite observations, Atmos. Res., 178–179, 580-589, doi:10.1016/j.atmosres.2016.05.010, 2016a.

Guo, J., Miao, Y., Zhang, Y., Liu, H., Li, Z., Zhang, W., He, J., Lou, M., Yan, Y., Bian, L., and Zhai, P.: The climatology of planetary boundary layer height in China derived from radiosonde and reanalysis data, Atmos. Chem. Phys., 16, 13309-13319, doi:10.5194/acp-16-13309-2016, 2016b.

Guo, S., Hu, M., Zamora, M.L., Peng, J., Shang, D., Zheng, J., Du, Z., Wu, Z., Shao, M., Zeng, L., Molina, M.J., and Zhang, R.: Elucidating severe urban haze formation in China, P. Natl. Acad. Sci. USA, 111, 17373-17378, doi:10.1073/pnas.1419604111, 2014.

Gustafsson, Ö., and Ramanathan, V.: Convergence on climate warming by black carbon aerosols, P. Natl. Acad. Sci. USA, 113, 4243-4245, doi:10.1073/pnas.1603570113, 2016.

Hara, Y., Uno, I., Shimizu, A., Sugimoto, N., Matsui, I., Yumimoto, K., Kurokawa, J.-i., Ohara, T., and Liu, Z.: Seasonal Characteristics of Spherical Aerosol Distribution in Eastern Asia:

Integrated Analysis Using Ground/Space-Based Lidars and a Chemical Transport Model, SOLA, 7, 121-124, doi:10.2151/sola.2011-031, 2011.

He, Q.S., Li, C.C., Mao, J.T., Lau, A.K.H., and Chu, D.A.: Analysis of aerosol vertical distribution and variability in Hong Kong, J. Geophys. Res., 113, D14211, doi:10.1029/2008JD009778, 2008.

Heese, B., Baars, H., Bohlmann, S., Althausen, D., and Deng, R.: Continuous vertical aerosol profiling with a multi-wavelength Raman polarization lidar over the Pearl River Delta, China, Atmos. Chem. Phys. Discuss., 2016, 1-25, doi:10.5194/acp-2016-733, 2016.

Huang, C., Chen, C.H., Li, L., Cheng, Z., Wang, H.L., Huang, H.Y., Streets, D.G., Wang, Y.J., Zhang, G.F., and Chen, Y.R.: Emission inventory of anthropogenic air pollutants and VOC species in the Yangtze River Delta region, China, Atmos. Chem. Phys., 11, 4105-4120, doi:10.5194/acp-11-4105-2011, 2011.

Huang, J., Huang, Z., Bi, J, Zhang, W., and Zhang, L.: Micro-Pulse Lidar Measurements of Aerosol Vertical Structure over the Loess Plateau, Atmos. Oceanic Sci. Lett., 1, 8-11, doi:10.1080/16742834.2008.11446756, 2008a.

Huang, J., Zhang, W., Zuo, J., Bi, J., Shi, J., Wang, X., Chang, Z., Huang, Z., Yang, S., Zhang, B., Wang, G., Feng, G., Yuan, J., Zhang, L., Zuo, H., Wang, S., Fu, C., and Chou, J.: An overview of the Semi-arid Climate and Environment Research Observatory over the Loess Plateau, Adv. Atmos. Sci., 25, 906-921, doi:10.1007/s00376-008-0906-7, 2008b.

Huang, J.P., Liu, J.J., Chen, B., and Nasiri, S.L.: Detection of anthropogenic dust using CALIPSO lidar measurements, Atmos. Chem. Phys., 15, 11653-11665, doi:10.5194/acp-15-11653-2015, 2015b.

Huang, Z., Huang, J., Bi, J., Wang, G., Wang, W., Fu, Q., Li, Z., Tsay, S.-C., and Shi, J.: Dust aerosol vertical structure measurements using three MPL lidars during 2008 China-U.S. joint dust field experiment, J. Geophys. Res., 115, D00K15, doi:10.1029/2009JD013273, 2010.

Huang, Z., Huang, J., Hayasaka, T., Wang, S., Zhou, T., and Jin, H.: Short-cut transport path for Asian dust directly to the Arctic: a case study, Environ. Res. Lett., 10, 114018, doi:http://dx.doi.org/10.1088/1748-9326/10/11/114018, 2015a.

Huneeus, N., Schulz, M., Balkanski, Y., Griesfeller, J., Prospero, J., Kinne, S., Bauer, S., Boucher, O., Chin, M., Dentener, F., Diehl, T., Easter, R., Fillmore, D., Ghan, S., Ginoux, P., Grini, A., Horowitz, L., Koch, D., Krol, M.C., Landing, W., Liu, X., Mahowald, N., Miller, R., Morcrette, J.J., Myhre, G., Penner, J., Perlwitz, J., Stier, P., Takemura, T., and Zender, C.S.: Global dust model intercomparison in AeroCom phase I, Atmos. Chem. Phys., 11, 7781-7816, doi:10.5194/acp-11-7781-2011, 2011.

Jia, R., Liu, Y.Z., Chen, B., Zhang, Z.J., and Huang, J.P.: Source and transportation of summer dust over the Tibetan Plateau, Atmos. Environ., 123, 210-219, doi:10.1016/j.atmosenv.2015.10.038, 2015.

Kandler, K., Lieke, K., Benker, N., Emmel, C., Kupper, M., Muller-Ebert, D., Ebert, M., Scheuvens, D., Schladitz, A., Schutz, L., and Weinbruch, S.: Electron microscopy of particles collected at Praia, Cape Verde, during the Saharan Mineral Dust Experiment: particle chemistry, shape, mixing state and complex refractive index, Tellus B, 63, 475-496, doi:10.1111/j.1600-0889.2011.00550.x, 2011.

Khalizov, A.F., Xue, H., and Zhang, R.: Enhanced light absorption and scattering by carbon soot aerosols internally mixed with sulfuric acid, J. Phys. Chem. 113, 1066–1074, doi: 10.1021/jp807531n, 2009.

Kipling, Z., Stier, P., Johnson, C. E., Mann, G. W., Bellouin, N., Bauer, S. E., Bergman, T., Chin, M., Diehl, T., Ghan, S. J., Iversen, T., Kirkevåg, A., Kokkola, H., Liu, X., Luo, G., van Noije, T., Pringle, K. J., von Salzen, K., Schulz, M., Seland, Ø., Skeie, R. B., Takemura, T., Tsigaridis, K., and Zhang, K.: What controls the vertical distribution of aerosol? Relationships between process sensitivity in HadGEM3–UKCA and inter-model variation from AeroCom Phase II, Atmos. Chem. Phys., 16, 2221-2241, doi:10.5194/acp-16-2221-2016, 2016.

Koffi, B., Schulz, M., Bréon, F.-M., Griesfeller, J., Winker, D., Balkanski, Y., Bauer, S., Berntsen, T., Chin, M., Collins, W.D., Dentener, F., Diehl, T., Easter, R., Ghan, S., Ginoux, P., Gong, S., Horowitz, L.W., Iversen, T., Kirkevåg, A., Koch, D., Krol, M., Myhre, G., Stier, P., and Takemura, T.: Application of the CALIOP layer product to

evaluate the vertical distribution of aerosols estimated by global models: AeroCom phase I results, J. Geophys. Res., 117, D10201, doi:10.1029/2011JD016858, 2012.

Lei, W., Zhang, R., McGivern, W. S., Derecskei-Kovacs, A., and North, S. W.: Theoretical Study of OH−O2−Isoprene Peroxy Radicals, J. Phys. Chem. A, 105, 471-477, doi:10.1021/jp0027039, 2001.

Li, G., Wang, Y., and Zhang, R.: Implementation of a two-moment bulk microphysics scheme to the WRF model to investigate aerosol-cloud interaction, J. Geophys. Res., 113, D15211, doi:10.1029/2007JD009361, 2008.

Li, J., Carlson, B. E., and Lacis, A. A.: Using single-scattering albedo spectral curvature to characterize East Asian aerosol mixtures, J. Geophys. Res., 120, 2037-2052, doi:10.1002/2014JD022433, 2015.

Li, Z., Chen, H., Cribb, M., Dickerson, R., Holben, B., Li, C., Lu, D., Luo, Y., Maring, H., Shi, G., Tsay, S.C., Wang, P., Wang, Y., Xia, X., Zheng, Y., Yuan, T., and Zhao, F.: Preface to special section on East Asian Studies of Tropospheric Aerosols: An International Regional Experiment (EAST-AIRE), J. Geophys. Res., 112, D22S00, doi:10.1029/2007JD008853, 2007.

Li, Z., Niu, F., Fan, J., Liu, Y., Rosenfeld, D., and Ding, Y.: Long-term impacts of aerosols on the vertical development of clouds and precipitation, Nat. Geosci., 4, 888-894, doi:10.1038/ngeo1313, 2011.

Liu, C., Shen X., Gao W., Liu P., and Sun Z.: Evaluation of CALIPSO aerosol optical depth using AERONET and MODIS data over China, In SPIE Optical Engineering Applications 2014 Oct 2 (pp. 92210F-92210F), International Society for Optics and Photonics, doi:10.1117/12.2058929, 2014.

Liu, X.H., Zhang, Y., Xing, J., Zhang, Q.A., Wang, K., Streets, D.G., Jang, C., Wang, W.X., and Hao, J.M.: Understanding of regional air pollution over China using CMAQ, part II. Process analysis and sensitivity of ozone and particulate matter to precursor emissions, Atmos. Environ., 44, 3719-3727, doi:10.1016/j.atmosenv.2010.03.036, 2010.

Liu, Z., Liu, D., Huang, J., Vaughan, M., Uno, I., Sugimoto, N., Kittaka, C., Trepte, C., Wang, Z., Hostetler, C., and Winker, D.: Airborne dust distributions over the Tibetan Plateau and surrounding areas derived from the first year of CALIPSO lidar observations, Atmos. Chem. Phys., 8, 5045-5060, doi:10.5194/acp-8-5045-2008, 2008.

Logan, T., Xi, B., Dong, X., Obrecht, R., Li, Z., and Cribb, M.: A study of Asian dust plumes using satellite, surface, and aircraft measurements during the INTEX-B field experiment, J. Geophys. Res., 115, D00K25, doi:10.1029/2010JD014134, 2010.

Logan, T., Xi, B., Dong, X., Li, Z., and Cribb, M.: Classification and investigation of Asian aerosol absorptive properties, Atmos. Chem. Phys., 13, 2253-2265, doi:10.5194/acp-13-2253-2013, 2013.

Luo, Y.X., Zheng, X.B., Zhao, T.L., and Chen, J.: A climatology of aerosol optical depth over China from recent 10 years of MODIS remote sensing data, Int. J. Climatol. 34, 863-870, doi:10.1002/joc.3728, 2014.

Ma, Z.W., Hu, X.F., Sayer, A.M., Levy, R., Zhang, Q., Xue, Y.G., Tong, S.L., Bi, J., Huang, L., and Liu, Y.: Satellite-Based Spatiotemporal Trends in PM2.5 Concentrations: China, 2004-2013, Environ. Health Persp., 124, 184-192, doi:10.1289/ehp.1409481, 2016.

Miao, Y., Hu, X.-M., Liu, S., Qian, T., Xue, M., Zheng, Y., and Wang, S.: Seasonal variation of local atmospheric circulations and boundary layer structure in the Beijing-Tianjin-Hebei region and implications for air quality, J. Adv. Model Earth Sy. , 7, 1602-1626, doi:10.1002/2015MS000522, 2015.

Mielonen, T., Arola, A., Komppula, M., Kukkonen, J., Koskinen, J., de Leeuw, G., and Lehtinen, K.: Comparison of CALIOP level 2 aerosol subtypes to aerosol types derived from AERONET inversion data, Geophys. Res. Lett., 36, L18804, doi:10.1029/2009GL039609, 2009.

Nemuc, A., Vasilescu, J., Talianu, C., Belegante, L., and Nicolae, D.: Assessment of aerosol's mass concentrations from measured linear particle depolarization ratio (vertically resolved) and simulations, Atmos. Meas. Tech., 6, 3243-3255, doi:10.5194/amt-6-3243-2013, 2013.

Nesbitt, S.W., Zhang, R., and Orville, R.E.: Seasonal and global NO_x production by lightning estimated from the Optical Transient Detector (OTD), Tellus B, 52, 1206-1215, doi: 10.1034/j.1600-0889.2000.01121.x, 2000.

Omar, A.H., Won, J.-G., Winker, D.M., Yoon, S.-C., Dubovik, O., and McCormick, M.P..: Development of global aerosol models using cluster analysis of Aerosol Robotic Network (AERONET) measurements, J. Geophys. Res., 110, D10S14, doi:10.1029/2004JD004874, 2005.

Omar, A.H., Winker, D.M., Vaughan, M.A., Hu, Y., Trepte, C.R., Ferrare, R.A., Lee, K.-P., Hostetler, C.A., Kittaka, C., Rogers, R.R., Kuehn, R.E., and Liu, Z.: The CALIPSO Automated Aerosol Classification and Lidar Ratio Selection Algorithm, J. Atmos. Ocean. Tech., 26, 1994-2014, doi:http://dx.doi.org/10.1175/2009JTECHA1231.1, 2009.

Pan, X., Uno, I., Hara, Y., Kuribayashi, M., Kobayashi, H., Sugimoto, N., Yamamoto, S., Shimohara, T., and Wang, Z.: Observation of the simultaneous transport of Asian mineral dust aerosols with anthropogenic pollutants using a POPC during a long-lasting dust event in late spring 2014, Geophys. Res. Lett., 42, 1593-1598, doi:10.1002/2014GL062491, 2015.

Papagiannopoulos, N., Mona, L., Alados-Arboledas, L., Amiridis, V., Baars, H., Binietoglou, I., Bortoli, D., D'Amico, G., Giunta, A., Guerrero-Rascado, J.L., Schwarz, A., Pereira, S., Spinelli, N., Wandinger, U., Wang, X., and Pappalardo, G.: CALIPSO climatological

products: evaluation and suggestions from EARLINET, Atmos. Chem. Phys., 16, 2341-2357, 2016, doi:10.5194/acp-16-2341-2016, 2016.

Peng, J., Hu, M., Guo, S., Du, Z., Zheng, J., Shang, D., Levy Zamora, M., Zeng, L., Shao, M., Wu, Y.-S., Zheng, J., Wang, Y., Glen, C.R., Collins, D.R., Molina, M.J., and Zhang, R.: Markedly enhanced absorption and direct radiative forcing of black carbon under polluted urban environments, P. Natl. Acad. Sci. USA, 113, 4266-4271, doi:10.1073/pnas.1602310113, 2016.

Petäjä, T., Järvi, L., Kerminen, V.M., Ding, A.J., Sun, J.N., Nie, W., Kujansuu, J., Virkkula, A., Yang, X., and Fu, C.B., Zilitinkevich, S., Kulmala, M.: Enhanced air pollution via aerosol-boundary layer feedback in China, Sci. Rep., 6, 18998, doi:10.1038/srep18998, 2016.

Porter, J.N. and Clarke, A.D.: Aerosol size distribution models based on in situ measurements, J. Geophys. Res., 102, 6035-6045, doi:10.1029/96JD03403, 1997.

Qi, Y., Ge, J., and Huang, J.: Spatial and temporal distribution of MODIS and MISR aerosol optical depth over northern China and comparison with AERONET, Chinese Sci. Bull. , 58, 2497-2506, doi:10.1007/s11434-013-5678-5, 2013.

Qiu, C., and Zhang, R.: Physiochemical Properties of AlkylaminiumSulfates: Hygroscopicity, Thermostability, and Density, Environ. Sci. Technol., 46, 4474-4480, doi:10.1021/es3004377, 2012.

Qiu, C., and Zhang, R.: Multiphase chemistry of atmospheric amines, Phys. Chem. Chem. Phys., 15, 5738-5752, doi:10.1039/C3CP43446J, 2013.

Rosenfeld, D., Sherwood, S., Wood, R., and Donner, L.: Climate Effects of Aerosol-Cloud Interactions, Science, 343, 379-380, doi:10.1126/science.1247490, 2014.

Sasano, Y. and Browell, E.V.: Light scattering characteristics of various aerosol types derived from multiple wavelength lidar observations, Appl. Optics, 28, 1670-1679, doi:10.1364/AO.28.001670, 1989.

Schleicher, N., Norra, S., Fricker, M., Kaminski, U., Chen, Y., Chai, F., Wang, S., Yu, Y., and Cen, K.: Spatio-temporal variations of black carbon concentrations in the Megacity Beijing, Environ. Pollut., 182, 392-401, doi:http://dx.doi.org/10.1016/j.envpol.2013.07.042, 2013.

Su, X., Cao, J., Li, Z., Lin, M., and Wang, G.: Column-Integrated Aerosol Optical Properties during Summer and Autumn of 2012 in Xi'an, China, Aerosol Air Qual. Res., 14, 850-861, doi:10.4209/aaqr.2013.03.0093, 2014.

Sugimoto, N., Matsui, I., Shimizu, A., Uno, I., Asai, K., Endoh, T., and Nakajima, T.: Observation of dust and anthropogenic aerosol plumes in the Northwest Pacific with a two-wavelength polarization lidar on board the research vessel Mirai, Geophys. Res. Lett., 29, 1901, doi:10.1029/2002GL015112, 2002.

Suh, I., Zhang, R., Molina, L. T., and Molina, M. J.: Oxidation Mechanism of Aromatic Peroxy and Bicyclic Radicals from OH−Toluene Reactions, J. Am. Chem. Soc., 125, 12655-12665, doi:10.1021/ja0350280, 2003.

Sugimoto, N. and Huang, Z.: Lidar methods for observing mineral dust, J. Meteor. Res., 28, 173-184, doi:10.1007/s13351-014-3068-9, 2014.

Takamura, T., Sasano, Y., and Hayasaka, T.: Tropospheric aerosol optical properties derived from lidar, sun photometer, and optical particle counter measurements, Appl. Opt., 33, 7132-7140, doi:10.1364/AO.33.007132, 1994.

Tao, M., Chen, L., Wang, Z., Tao, J., Che, H., Wang, X., and Wang, Y.: Comparison and evaluation of the MODIS Collection 6 aerosol data in China, J. Geophys. Res., 120, 6992-7005, doi:10.1002/2015JD023360, 2015.

Tian, P., Cao, X., Liang, J., Zhang, L., Yi, N., Wang, L., and Cheng, X.: Improved empirical mode decomposition based denoising method for lidar signals, Opt. Commun. , 325, 54-59, doi:10.1016/j.optcom.2014.03.083, 2014.

Wang, G., Zhang, R., Gomez, M.E., Yang, L., Zamora, M.L., Hu, M., Lin, Y., Peng, J., Guo, S., Meng, J., Li, J., Cheng, C., Hu, T., Ren, Y., Wang, Y., Gao, J., Cao, J., An, Z., Zhou, W., Li, G., Wang, J., Tian, P., Marrero-Ortiz, W., Secrest, J., Du, Z., Zheng, J., Shang, D., Zeng, L., Shao, M., Wang, W., Huang, Y., Wang, Y., Zhu, Y., Li, Y., Hu, J., Pan, B., Cai, L., Cheng, Y., Ji, Y., Zhang, F., Rosenfeld, D., Liss, P.S., Duce, R.A., Kolb, C.E., Molina

M.J.: Persistent sulfate formation from London Fog to Chinese Haze, Proc. Natl. Acad. Sci. USA, 113, 13630–13635, doi/10.1073/pnas.1616540113, 2016.

Wang, H., Zhang, L., Cao, X., Zhang, Z., and Liang, J.: A-Train satellite measurements of dust aerosol distributions over northern China, J. Quant. Spectrosc. Ra., 122, 170-179, doi:10.1016/j.jqsrt.2012.08.011, 2013b.

Wang, S., Zhang, Q., Martin, R.V., Philip, S., Liu, F., Li, M., Jiang, X., and He, K.: Satellite measurements oversee China's sulfur dioxide emission reductions from coal-fired power plants, Environ. Res. Lett., 10, 114015, doi:10.1088/1748-9326/10/11/114015, 2015.

Wang, Y., Wan, Q., Meng, W., Liao, F., Tan, H., and Zhang, R.: Long-term impacts of aerosols on precipitation and lightning over the Pearl River Delta megacity area in China, Atmos. Chem. Phys. 11, 12421–12436, doi:10.5194/acp-11-12421-2011, 2011.

Wang, Y., Khalizov, A., Levy, M., and Zhang, R.: New Directions: Light absorbing aerosols and their atmospheric impacts, Atmos. Environ., 81, 713-715, doi:10.1016/j.atmosenv.2013.09.034, 2013a.

Wang, Y., Zhang, R. Y., and Saravanan, R.: Asian pollution climatically modulates mid-latitude cyclones following hierarchical modelling and observational analysis, Nat. Commun., 5, doi:10.1038/ncomms4098, 2014.

Winker, D.M., Vaughan, M.A., Omar, A., Hu, Y.X., Powell, K.A., Liu, Z.Y., Hunt, W.H., and Young, S.A.: Overview of the CALIPSO Mission and CALIOP Data Processing

Algorithms, J. Atmos. Ocean. Tech., 26, 2310-2323, doi:http://dx.doi.org/10.1175/2009JTECHA1281.1, 2009.

Winker, D.M., Tackett, J.L., Getzewich, B.J., Liu, Z., Vaughan, M.A., and Rogers, R.R.: The global 3-D distribution of tropospheric aerosols as characterized by CALIOP, Atmos. Chem. Phys., 13, 3345-3361, doi:10.5194/acp-13-3345-2013, 2013.

Wu, D., Zhou, J., Liu, D., Wang, Z., Zhong, Z., Xie, C., Qi, F., Fan, A., and Wang, Y.: 12-year lidar Observations of Tropospheric Aerosol over Hefei (31.9°N, 117.2°E), China, J. Opt. Soc. Koear, 15, 90-95, doi:10.3807/JOSK.2011.15.1.090, 2011.

Wu, G., Li, Z., Fu, C., Zhang, X., Zhang, R., Zhang, R., Zhou, T., Li, J., Li, J., Zhou, D., Wu, L., Zhou, L., He, B., and Huang, R.: Advances in studying interactions between aerosols and monsoon in China, Sci. China: Earth Sci., 59, 1–16, doi: 10.1007/s11430-015-5198-z, 2016.

Wu, M., Wu, D., Fan, Q., Wang, B.M., Li, H.W., and Fan, S.J.: Observational studies of the meteorological characteristics associated with poor air quality over the Pearl River Delta in China, Atmos. Chem. Phys., 13, 10755-10766, doi:10.5194/acp-13-10755-2013, 2013.

Xie, C.B., Nishizawa, T., Sugimoto, N., Matsui, I., and Wang, Z.F.: Characteristics of aerosol optical properties in pollution and Asian dust episodes over Beijing, China, Appl. Optics, 47, 4945-4951, doi:10.1364/AO.47.004945, 2008.

Xie, S., Liu, X., Zhao, C., and Zhang, Y.: Sensitivity of CAM5-Simulated Arctic Clouds and Radiation to Ice Nucleation Parameterization, J. Climate., 26(16), 5981-5999, doi:10.1175/jcli-d-12-00517.1, 2013.

Xin, J., Wang, Y., Pan, Y., Ji, D., Liu, Z., Wen, T., Wang, Y., Li, X., Sun, Y., Sun, J., Wang, P., Wang, G., Wang, X., Cong, Z., Song, T., Hu, B., Wang, L., Tang, G., Gao, W., Guo, Y., Miao, H., Tian, S., and Wang, L.: The Campaign on Atmospheric Aerosol Research Network of China: CARE-China, B. Am. Meteorol. Soc., 96, 1137-1155, doi:http://dx.doi.org/10.1175/BAMS-D-14-00039.1, 2015.

Xu, Z., Xue, L. K., Wang, T., Xia, T., Gao, Y., Louie, P. K. K., and Luk, C. W. Y.: Measurements of Peroxyacetyl Nitrate at a Background Site in the Pearl River Delta Region: Production Efficiency and Regional Transport, Aerosol Air Qual. Res., 15, 833-841, doi:10.4209/aaqr.2014.11.0275, 2015.

Yang, X., Zhao, C., Guo, J., and Wang, Y.: Intensification of aerosol pollution associated with its feedback with surface solar radiation and winds in Beijing, J. Geophys. Res., 121, 4093-4099, doi:10.1002/2015JD024645, 2016.

Yu, H., Chin, M., Winker, D.M., Omar, A.H., Liu, Z., Kittaka, C., and Diehl, T.: Global view of aerosol vertical distributions from CALIPSO lidar measurements and GOCART simulations: Regional and seasonal variations, J. Geophys. Res., 115, D00H30, doi:10.1029/2009JD013364, 2010.

Yue, D. L., Hu, M., Zhang, R. Y., Wang, Z. B., Zheng, J., Wu, Z. J., Wiedensohler, A., He, L. Y., Huang, X. F., and Zhu, T.: The roles of sulfuric acid in new particle formation and growth in the mega-city of Beijing, Atmos. Chem. Phys., 10, 4953-4960, doi:10.5194/acp-10-4953-2010, 2010.

Zhao, C., and Garrett T. J.: Effects of Arctic haze on surface cloud radiative forcing, Geophys. Res. Lett., 42(2), 557-564, doi:10.1002/2014GL062015, 2015.

Zhao, J., Levitt, N. P., Zhang, R., and Chen, J.: Heterogeneous Reactions of Methylglyoxal in Acidic Media: Implications for Secondary Organic Aerosol Formation, Environ. Sci. Technol., 40, 7682-7687, doi:10.1021/es060610k, 2006.

Zhang, D., Zhang, R., Park, J., and North, S. W.: HydroxyPeroxy Nitrites and Nitrates from OH Initiated Reactions of Isoprene, J. Am. Chem. Soc., 124, 9600-9605, doi:10.1021/ja0255195, 2002.

Zhang, D., and Zhang, R.: Laboratory Investigation of Heterogeneous Interaction of Sulfuric Acid with Soot, Environ. Sci. Technol., 39, 5722-5728, doi:10.1021/es050372d, 2005.

Zhang, R., Leu, M.T., and Keyser, L.F.: Heterogeneous chemistry of HONO on liquid sulfuric acid: A new mechanism of chlorine activation on stratospheric sulfate aerosols, J. Phys. Chem., 100, 339-345, doi:10.1021/jp952060a, 1996.

Zhang, R., Li, G., Fan, J., Wu, D. L., and Molina, M. J.: Intensification of Pacific storm track linked to Asian pollution, Proc. Natl. Acad. Sci. U.S.A., 104, 5295-5299, doi:10.1073/pnas.0700618104, 2007.

Zhang, R., Khalizov, A. F., Pagels, J., Zhang, D., Xue, H., and McMurry, P. H.: Variability in morphology, hygroscopicity, and optical properties of soot aerosols during atmospheric processing, Proc. Natl. Acad. Sci. U.S.A., 105, 10291-10296, doi:10.1073/pnas.0804860105, 2008.

Zhang, R., Wang, G.H., Guo, S., Zarnora, M.L., Ying, Q., Lin, Y., Wang, W.G., Hu, M., and Wang, Y.: Formation of Urban Fine Particulate Matter, Chem. Rev., 115, 3803-3855, doi:10.1021/acs.chemrev.5b00067, 2015.

Zhang, X.Y., Wang, Y.Q., Niu, T., Zhang, X.C., Gong, S.L., Zhang, Y.M., and Sun, J.Y.: Atmospheric aerosol compositions in China: spatial/temporal variability, chemical signature, regional haze distribution and comparisons with global aerosols, Atmos. Chem. Phys., 12, 779-799, doi:10.5194/acp-12-779-2012, 2012.

Zhang, Y. and Cao, F.: Fine particulate matter (PM2.5) in China at a city level, Sci. Rep., 5, 14884, doi:10.1038/srep14884, 2015.

Zhou, T., Huang, J., Huang, Z., Liu, J., Wang, W., and Lin, L.: The depolarization–attenuated backscatter relationship for dust plumes, Opt. Express, 21, 15195-15204, doi:10.1364/OE.21.015195, 2013.

Table 1. Classification of the study regions.

Region	Abbreviation	Latitude-longitude range
Loess Plateau	LP	34.0-38.0° N, 103.0-112.0° E
North China Plain	NCP	34.0-41.0° N, 113.0-119.0° E
Northeast China Plain	NEP	43.0-49.0° N, 120.0-130.0° E
Pearl River Delta	PRD	21.5-25.0° N, 111.0-116.0° E
Sichuan Basin	SB	28.0-33.0° N, 103.0-110.0° E
Taklimakan Desert	TD	37.0-42.0° N, 78.0-88.0° E
Tibetan Plateau	TP	30.0-36.0° N, 80.0-100.0° E
Yangtze River Delta	YRD	28.0-33.0° N, 116.0-122.0° E

Table 2. Ratio of the AOD within 1.5 km height above the ground to the total column AOD (%).

	TD	TP	LP	NEP	SB	NCP	YRD	PRD	Average
MAM	71.2	61.0	61.9	58.8	61.1	63.7	65.8	48.6	61.5
JJA	58.4	64.0	68.9	71.2	56.7	70.0	74.8	75.6	67.5
SON	74.5	65.6	79.7	74.3	72.9	81.3	84.4	83.0	77.0
DJF	89.0	65.9	82.0	78.1	77.5	82.8	83.2	82.8	80.2

Figure Captions

Figure 1. Study regions (square boxes) and AERONET sites (triangles) over a 1.0° × 2.5° latitude–longitude gridded surface elevation.

Figure 2. Aerosol extinction coefficient profiles from the ground-based NIES lidar and CALIOP observations over SACOL from October 2009 to August 2012: (a) spring; (b) summer; (c) autumn; and (d) winter. Altitudes of CALIOP observations are transferred to heights above the ground level of SACOL. The left and right boundaries of the light grey shadowed area depict the NIES lidar extinction coefficient averages with one standard deviation. The NIES lidar aerosol extinction coefficients were derived using an AOD-constrained retrieval method.

Figure 3. Seasonal AOD with a 1.0° ×2.5° latitude-longitude grid over China derived from CALIOP observations from June 2006 to January 2016.

Figure 4. Scatter plots of the layer-integrated aerosol color ratios versus the layer-integrated aerosol depolarization ratios for the regions: (a) Taklimakan Desert (TD); (b) Tibetan Plateau (TP); (c) Loess Plateau (LP); (d) Northeast China Plain (NEP); (e) Sichuan Basin (SB); (f) North China Plain (NCP); (g) Yangtze River Delta (YRD); and (h) Pearl River Delta (PRD).

Figure 5. Seasonal average layer-integrated aerosol color ratios versus layer-integrated aerosol depolarization ratios over the eight representative study regions in China.

Figure 6. The AERONET observed Ångström exponent versus AOD for (a) Hexi Corridor of Gansu (desert region); (b) the Tibetan Plateau (TP); (c) the Loess Plateau (LP); (d) the North China Plain (NCP); (e) the Yangtze River Delta (YRD); and (f) the Pearl River Delta (PRD). Similarly to Fig. 4, the color represents the number density of the Ångström exponent versus AOD data points.

Figure 7. Seasonal aerosol size distribution (a, c, e, and g) and spectral SSA (b, d, f, and h) in the LP, NCP, YRD and PRD regions, respectively.

Figure 8. (a) Volume size distribution, (b) spectral single scattering albedo (SSA) for dust-dominant aerosols (SACOL in spring), anthropogenic aerosols (Beijing and Taihu in summer), and aerosols of mixed type (spring Beijing) derived from the long-term AERONET observations.

Figure 9. Classification of the AERONET sites representing dust (SACOL in spring), anthropogenic aerosols (Beijing and Taihu in summer), and aerosols of the mixed types (Beijing in spring).

Figure 10. Aerosol extinction coefficient profiles for the following regions: (a) the Taklimakan Desert (TD); (b) the Tibetan Plateau (TP); (c) the Loess Plateau (LP); (d) the Northeast China Plain (NEP); (e) the Sichuan Basin (SB); (f) the North China Plain (NCP); (g) the Yangtze River Delta (YRD); and (h) the Pearl River Delta (PRD). The height is defined as the altitude above the sea-level.

Figure 11. Extinction lapse rates within 1.5 km above the ground. For the profiles where the extinction maximum is not reached at the bottom (such as the profiles for the Sichuan Basin because of the topography), the extinction lapse rates are calculated within 1.5 km above the height of the maximum extinctions.

5

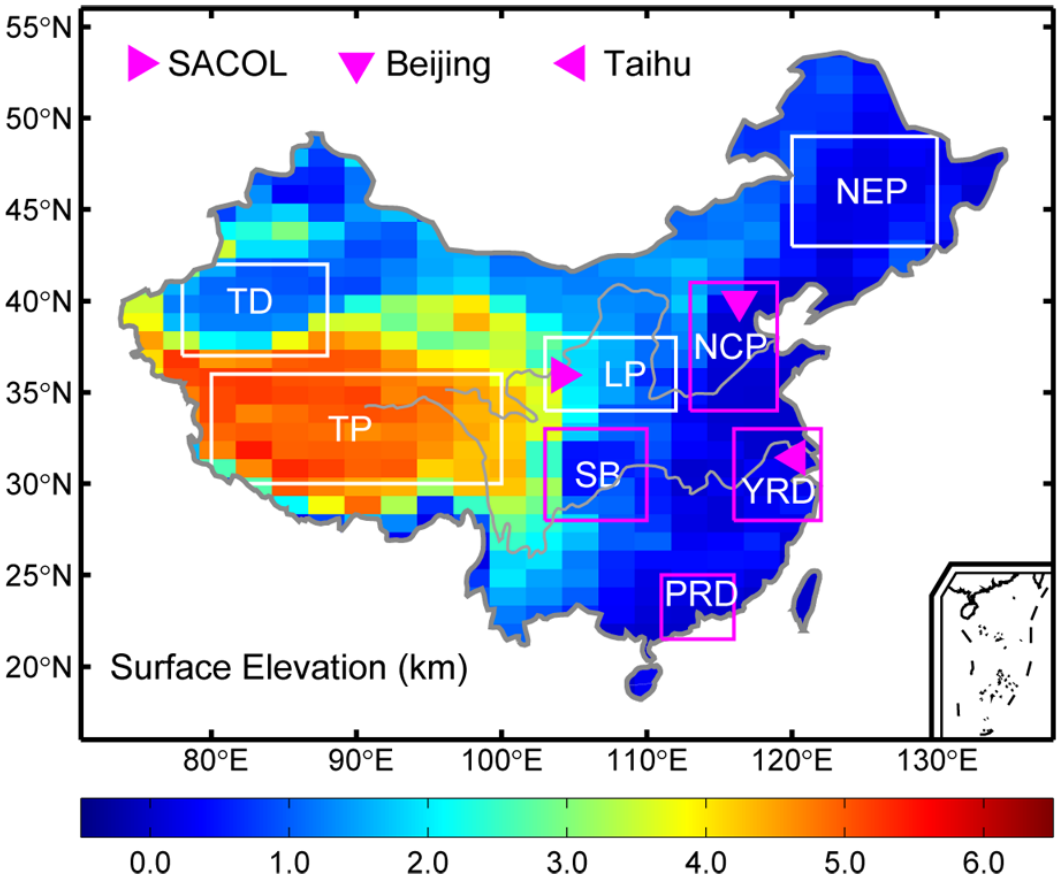
55°N
50°N
45°N
40°N
35°N
30°N
25°N
20°N
SACOL
Beijing
Taihu
NEP
TD
NCP
LP
TP
SB
YRD
PRD
Surface Elevation (km)
80°E
90°E
100°E
110°E
120°E
130°E
0.0
1.0
2.0
3.0
4.0
5.0
6.0

Figure 1.

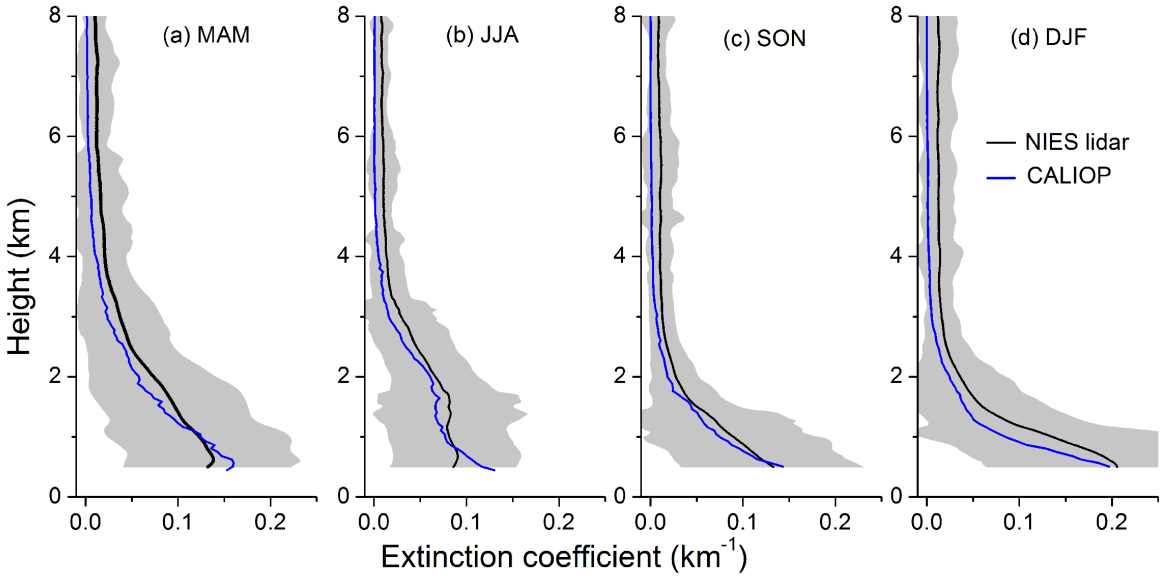
(a) MAM
(b) JJA
(c) SON
(d) DJF
NIES lidar
CALIOP
Height (km)
Extinction coefficient (km-1)
0
2
4
6
8
0.0
0.1
0.2

Figure 2.

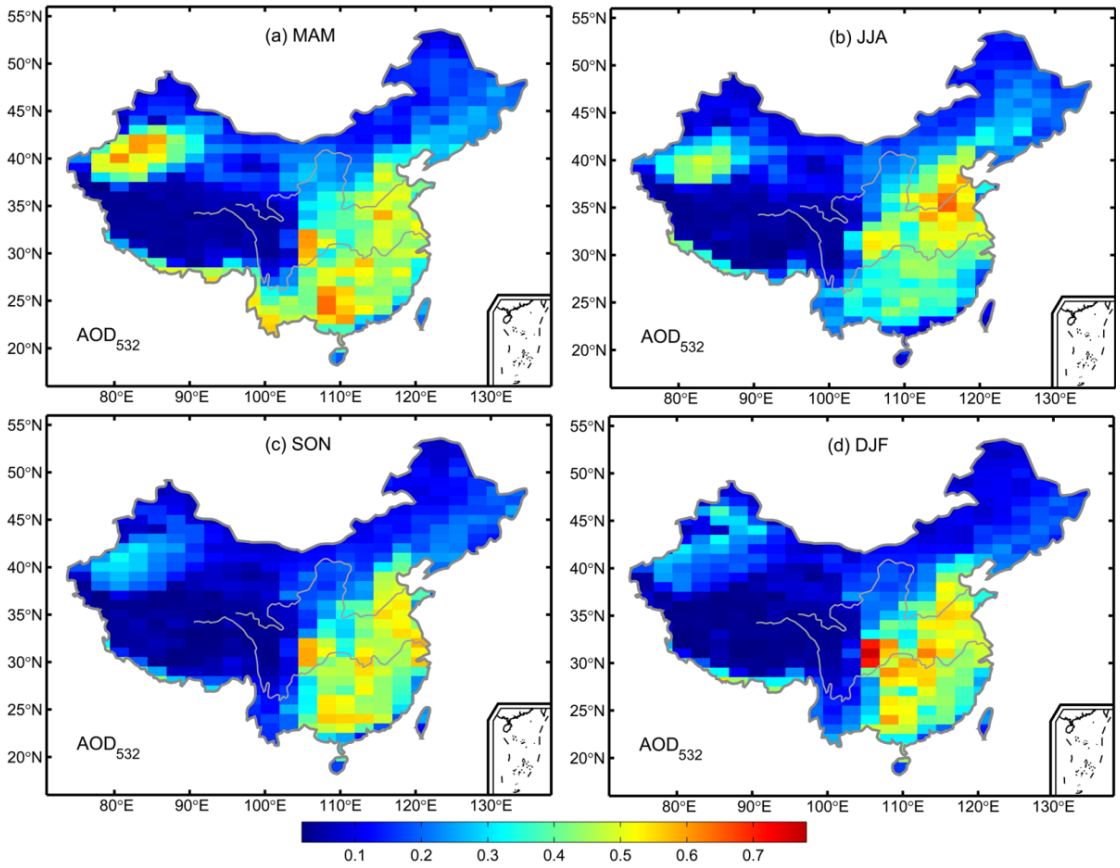
(a) MAM
(b) JJA
(c) SON
(d) DJF
AOD532
55°N
50°N
45°N
40°N
35°N
30°N
25°N
20°N
80°E
90°E
100°E
110°E
120°E
130°E
0.1
0.2
0.3
0.4
0.5
0.6
0.7

Figure 3.

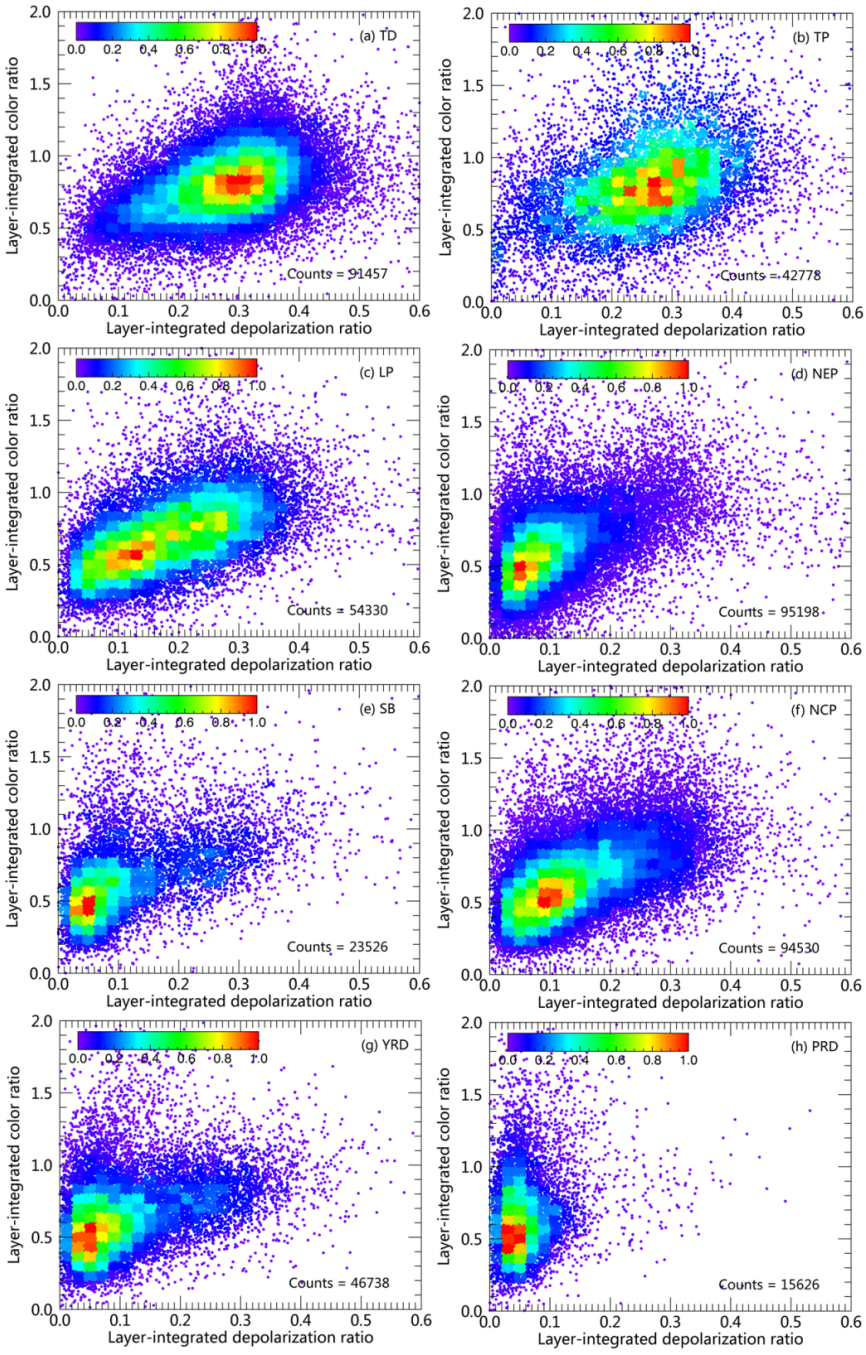
(a) TD
Counts = 91457
(b) TP
Counts = 42778
(c) LP
Counts = 54330
(d) NEP
Counts = 95198
(e) SB
Counts = 23526
(f) NCP
Counts = 94530
(g) YRD
Counts = 46738
(h) PRD
Counts = 15626
Layer-integrated color ratio
Layer-integrated depolarization ratio

Figure 4.

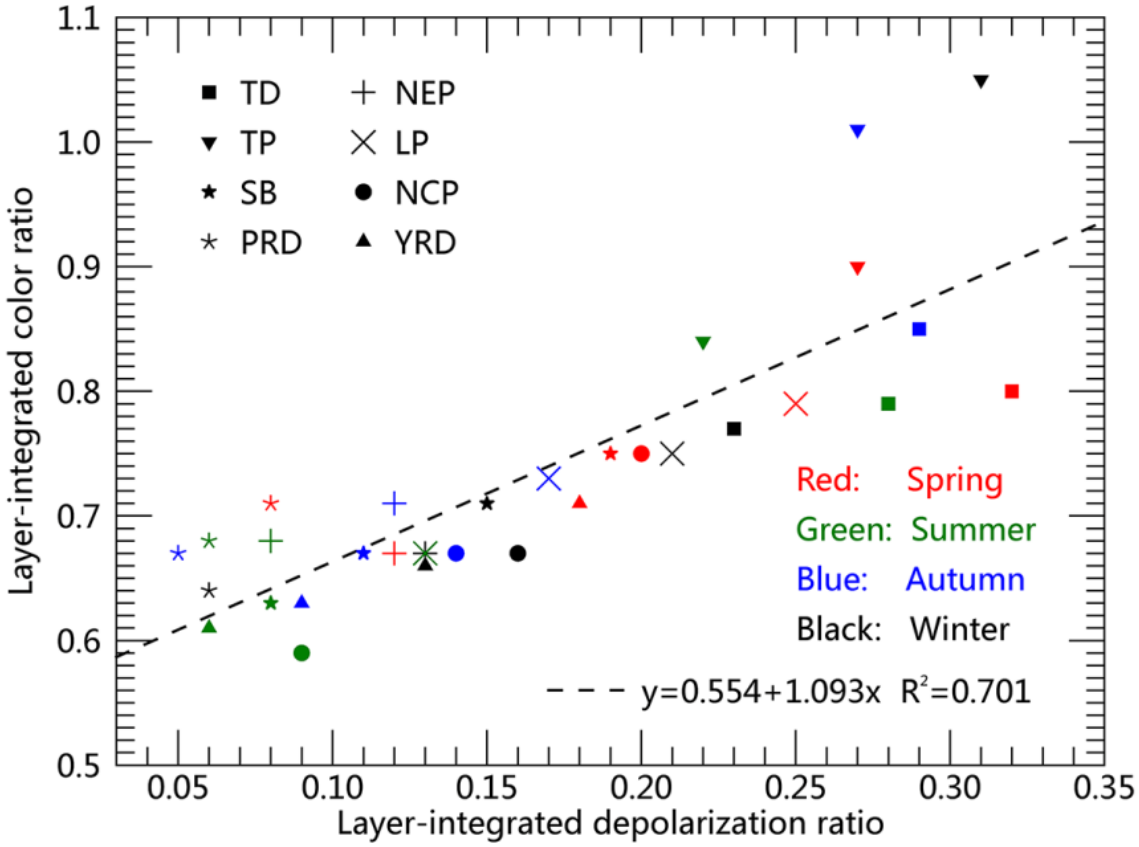
TD
TP
SB
PRD
NEP
LP
NCP
YRD
Red: Spring
Green: Summer
Blue: Autumn
Black: Winter
y=0.554+1.093x R²=0.701
Layer-integrated color ratio
Layer-integrated depolarization ratio
1.1
1.0
0.9
0.8
0.7
0.6
0.5
0.05
0.10
0.15
0.20
0.25
0.30
0.35

Figure 5.

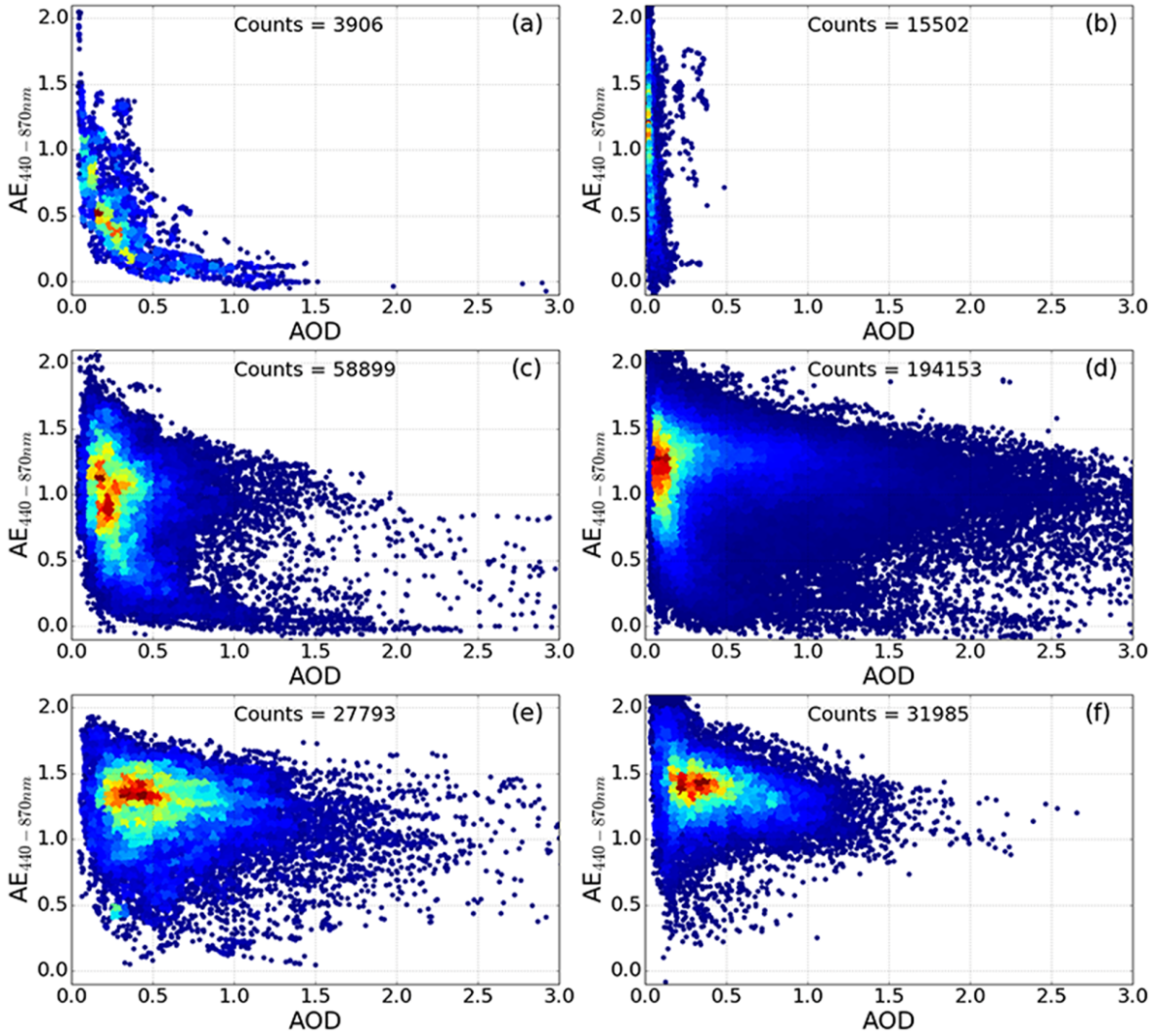
Counts = 3906
(a)
Counts = 15502
(b)
Counts = 58899
(c)
Counts = 194153
(d)
Counts = 27793
(e)
Counts = 31985
(f)
$AE_{440-870nm}$
AOD

Figure 6.

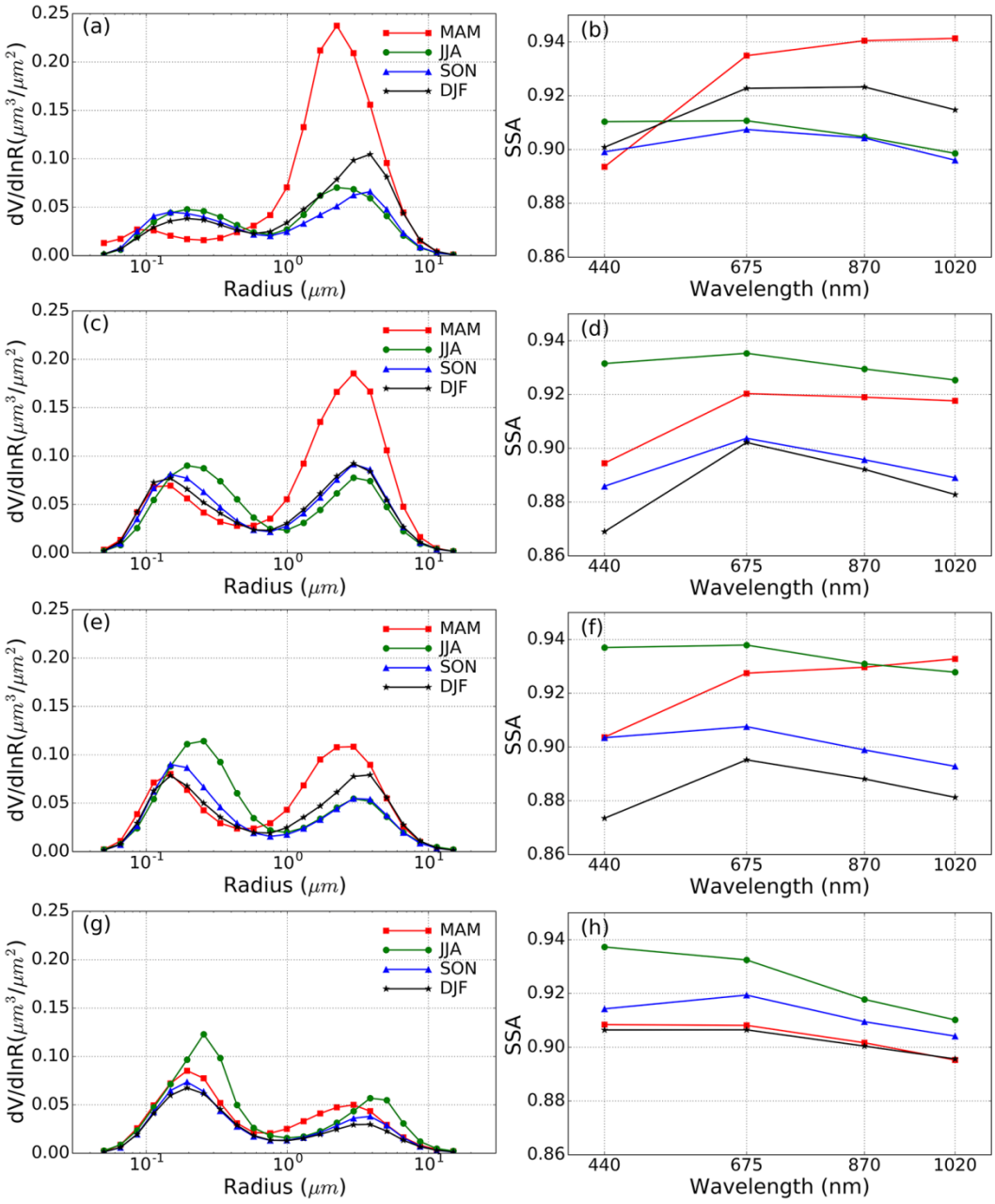
(a)
(b)
(c)
(d)
(e)
(f)
(g)
(h)
MAM
JJA
SON
DJF
dV/dlnR($\mu m^3/\mu m^2$)
Radius (μm)
SSA
Wavelength (nm)
0.25
0.20
0.15
0.10
0.05
0.00
10^{-1}
10^{0}
10^{1}
0.94
0.92
0.90
0.88
0.86
440
675
870
1020

Figure 7.

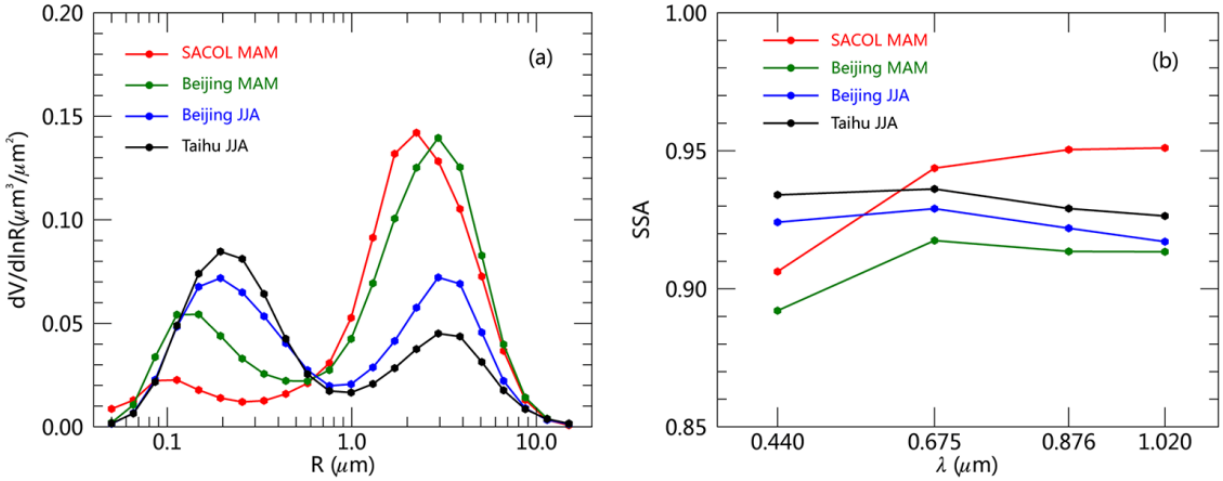
SACOL MAM
Beijing MAM
Beijing JJA
Taihu JJA
(a)
dV/dlnR(μm³/μm²)
R (μm)
(b)
SSA
λ (μm)

Figure 8.

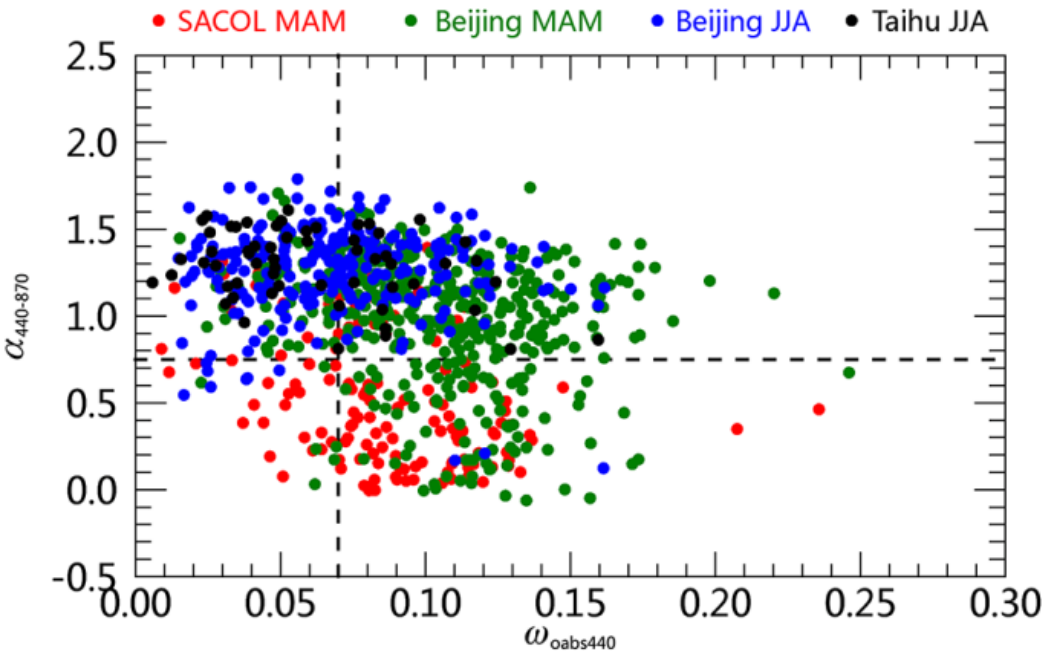
SACOL MAM
Beijing MAM
Beijing JJA
Taihu JJA
2.5
2.0
1.5
1.0
0.5
0.0
-0.5
$\alpha_{440\text{-}870}$
0.00
0.05
0.10
0.15
0.20
0.25
0.30
$\omega_{oabs440}$

Figure 9.

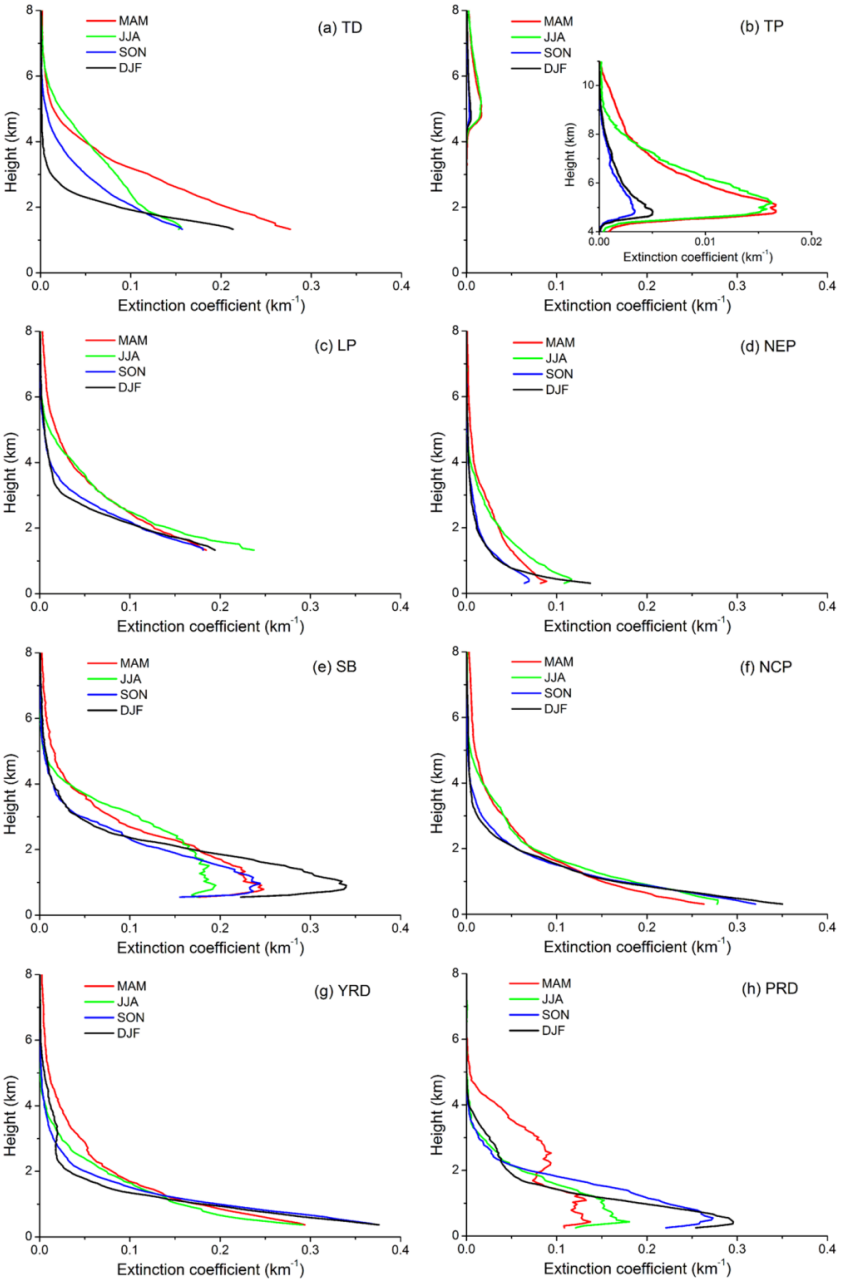
(a) TD
(b) TP
(c) LP
(d) NEP
(e) SB
(f) NCP
(g) YRD
(h) PRD
MAM
JJA
SON
DJF
Height (km)
Extinction coefficient (km^{-1})

Figure 10.

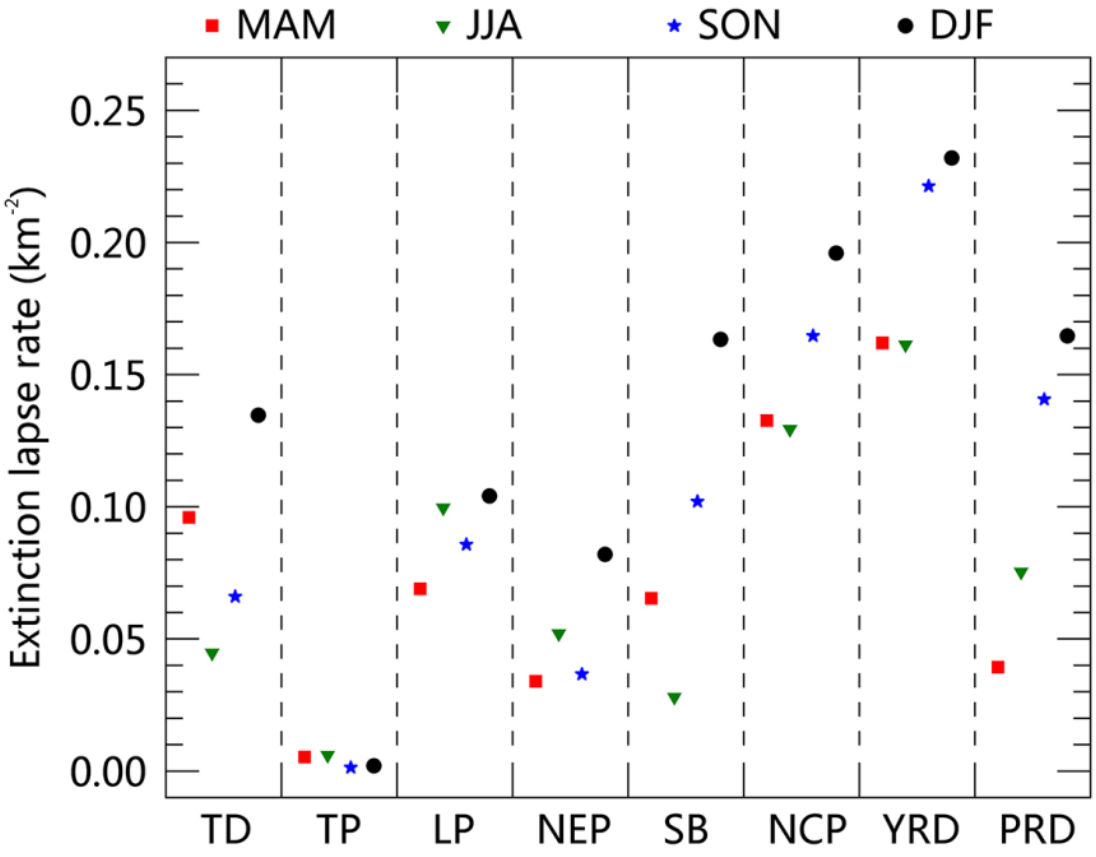
MAM
JJA
SON
DJF
Extinction lapse rate (km-2)
0.25
0.20
0.15
0.10
0.05
0.00
TD
TP
LP
NEP
SB
NCP
YRD
PRD

Figure 11.